

# Detection, analysis and removal of glitches from InSight's seismic data from Mars

John-Robert Scholz<sup>1</sup>, Rudolf Widmer-Schmidrig<sup>2</sup>, Paul Davis<sup>3</sup>, Philippe Lognonné<sup>4</sup>, Baptiste Pinot<sup>5</sup>, Raphaël F. Garcia<sup>5</sup>, Francis Nimmo<sup>6</sup>, Kenneth Hurst<sup>7</sup>, Salma Barkaoui<sup>4</sup>, Sébastien de Raucourt<sup>4</sup>, Laurent Pou<sup>6</sup>, Guénoé Mainsant<sup>5</sup>, Nicolas Compaire<sup>5</sup>, Arthur Cuvier<sup>8</sup>, Éric Beucler<sup>8</sup>, Mickaël Bonnin<sup>8</sup>, Rakshit Joshi<sup>1</sup>, Eléonore Stutzmann<sup>4</sup>, Martin Schimmel<sup>9</sup>, Anna Horleston<sup>10</sup>, Maren Böse<sup>11</sup>, Savas Ceylan<sup>13</sup>, John Clinton<sup>11</sup>, Martin van Driel<sup>13</sup>, Taichi Kawamura<sup>4</sup>, Amir Khan<sup>12,13</sup>, Simon C. Stähler<sup>13</sup>, Domenico Giardini<sup>13</sup>, Constantinos Charalambous<sup>14</sup>, Alexander E. Stott<sup>14</sup>, William T. Pike<sup>14</sup>, Ulrich R. Christensen<sup>1</sup>, W. Bruce Banerdt<sup>7</sup>

<sup>1</sup>Max Planck Institute for Solar System Research, Justus-von-Liebig-Weg 3, 37077 Göttingen, Germany

<sup>2</sup>Black Forest Observatory, Institute of Geodesy, Stuttgart University, Heubach 206, D-77709 Wolfach, Germany

<sup>3</sup>Department of Earth, Planetary, and Space Sciences, University of California Los Angeles, CA90095, USA

<sup>4</sup>Université de Paris, Institut de physique du globe de Paris, CNRS, F-75005 Paris, France

<sup>5</sup>Institut Supérieur de l'Aéronautique et de l'Espace SUPAERO, 10 Avenue Edouard Belin, 31400 Toulouse, France

<sup>6</sup>Dept. of Earth and Planetary Sciences, University of California Santa Cruz, Santa Cruz, CA 95064, USA

<sup>7</sup>Jet Propulsion Laboratory, California Institute of Technology, Pasadena, CA 91109, USA

<sup>8</sup>Laboratoire de planétologie et géodynamique, CNRS UMR 6112, Université de Nantes, Université d'Angers, France

<sup>9</sup>Institute of Earth Sciences Jaume Almera – CSIC, Barcelona, Spain

<sup>10</sup>School of Earth Sciences, University of Bristol, Wills Memorial Building, Queens Road, Bristol BS8 1RJ, UK

<sup>11</sup>Swiss Seismological Service (SED), ETH Zurich, Sonneggstr. 5, 8092 Zurich, Switzerland

<sup>12</sup>Institute of Theoretical Physics, University of Zurich, Zurich, Switzerland

<sup>13</sup>Institute of Geophysics, ETH Zürich, Sonneggstrasse 5, 8092 Zürich, Switzerland

<sup>14</sup>Department of Electrical and Electronic Engineering, Imperial College London, South Kensington Campus, London,

SW7 2AZ, United Kingdom

## Key Points:

- Glitches represent small steps in the recorded acceleration
- Glitches are mostly due to relaxations of thermal stresses and instrument tilt
- We provide a toolbox to automatically detect and remove glitches

---

Corresponding author: John-Robert Scholz, [scholz@mps.mpg.de](mailto:scholz@mps.mpg.de)

## Abstract

The SEIS instrument package with the three very broad-band and three short period seismic sensors is installed on the surface on Mars as part of NASA’s InSight Discovery mission. When compared to terrestrial installations, SEIS is deployed in a very harsh wind and temperature environment that leads to inevitable degradation for the quality of the recorded data. One ubiquitous artifact in the raw data is an abundance of transient one-sided pulses often accompanied by high-frequency precursors. These pulses, which we term “glitches”, can be modeled as the response of the instrument to a step in acceleration, while the precursors can be modeled as the response to a simultaneous step in displacement. We attribute the glitches primarily to SEIS-internal stress relaxations caused by the large temperature variations to which the instrument is exposed during a Martian day. Only a small fraction of glitches correspond to a motion of the SEIS package as a whole, and they are all due to minuscule instrument tilts. In this study, we focus on the analysis of the glitch+precursor phenomenon and present how these signals can be automatically detected and removed from SEIS’ raw data. As glitches affect many standard seismological analysis methods such as receiver functions or spectral decomposition, we anticipate that studies of Martian seismicity as well as studies of the internal structure of Mars should benefit from deglitched seismic data.

## Plain Language Summary

The SEIS instrument package with two fully equipped seismometers is installed on the surface of Mars as part of NASA’s InSight Discovery mission. When compared to terrestrial installations, SEIS is more exposed to wind and strong daily temperature changes that leads to inevitable degradation in the quality of the recorded data. Whilst we observe many types of transient noise caused by these conditions, there is one that occurs in abundance and has strong implications for the typical seismic data analysis. These signals, that we term “glitches”, show in the recorded data as one-sided pulses with a duration depending on the response of the seismometer to the recorded acceleration. Glitches are furthermore often preceded by high-frequency precursors that last a few seconds. We show that glitches can be understood as step-like changes in the acceleration sensed by the seismometers and precursors as step-like changes in the displacement sensed by the seismometers. We attribute glitches primarily to SEIS-internal stress relaxations caused by the large temperature variations to which the instrument is exposed during a Martian day. Only a small fraction of glitches correspond to a motion of the SEIS instrument and they are all due to minuscule instrument tilts. In this study, we focus on the analysis of the glitch+precursor phenomenon and present how these signals can be automatically detected and removed from SEIS’ data. As glitches affect many standard seismological analysis methods, we anticipate that studies of Martian seismicity as well as studies of the internal structure of Mars should benefit from deglitched seismic data.

## 1 Introduction

InSight (Interior Exploration using Seismic Investigations, Geodesy and Heat Transport) landed successfully on Mars on November 26, 2018 (Sol 0). Since February 9, 2019 (Sol 73), InSight’s main scientific instrument SEIS (Seismic Experiment for Internal Structure) is recording seismic data in its operational configuration (Banerdt et al., 2020). The SEIS package (Lognonné et al., 2019), whose network and station code for the scientific data is XB.ELYSE, consists of two three-component seismometers; one being very broadband (VBB) with a corner period of 16 seconds, and one being short-period (SP) with a corner period of 35 seconds. Notwithstanding the corner periods, the noise floor of the two instruments is equivalent only above 4 Hz while it is about  $\sim 30$  dB lower for the VBB at frequencies of 0.1 Hz and less. The VBB is therefore the main instrument to detect distant Marsquakes, while the SP is used to cover the frequency range of  $\sim 5$ –50 Hz for more detailed analysis of regional events and lander-induced signals. Both seismometers have non-orthogonal sensor orientations (Fig. 1a,c). To date, all six seismic components as well as the acquisition system have functioned nominally, exceeded mission requirements, and delivered unprecedented seismic data from the surface of Mars (InSight Mars SEIS Data Service, 2019). In addition to seismic signals of natural and artificial origins, i.e. Marsquakes (Lognonné et al., 2020; Giardini et al., 2020; for Marsquake catalog see: InSight Marsquake Service, 2020) and records from the HP<sup>3</sup>-instrument hammering sessions (Spohn et al., 2018), respectively, these data show a variety of non-seismic signals whose origin is not always clear but under investigation. Amongst the most prominent and abundant types of these non-seismic

83 signals are what we termed a "glitch". Glitches influence many of the standard seismological methods  
 84 such as receiver functions, polarization analyses and spectral decomposition and hence their correct  
 85 treatment is of high importance. The present study focuses on the detection, analysis and removal of  
 86 glitches and extends Supplement V of Lognonné et al. (2020).

## 87 Glitches

88 A glitch (Fig. 1b,d) is a particular type of transient instrumental self-noise that, in the raw time  
 89 series data, appear as a high amplitude, one-sided pulse with a duration controlled by the respective  
 90 seismometer's transfer function. For the VBB sensors, which have 76% of critical damping, glitches  
 91 have a fast rise time followed by an exponential decay with a small ( $\sim 9\%$ ) overshoot before, almost,  
 92 returning to the baseline after  $\sim 25$  s. For the SP sensors, that are overdamped with 110% of critical  
 93 damping, glitches have a similar rise time followed by a decay that takes the form of a near critically  
 94 damped sinusoidal before, almost, returning to the baseline after  $\sim 40$  s. Glitches may also occur  
 95 before a previous glitch has sufficiently decayed. The highest order of such "poly-glitches" we observe  
 96 to date is four. Glitches (and poly-glitches) can occur on all three VBB and all three SP sensors  
 97 simultaneously but there are many examples where a glitch occurs on only one component. They  
 98 occur at all times of the Martian day (sol, around 24h 40m) but are observed more frequently during  
 99 the quiet parts in the early evening and night. This is due the decreased seismic noise level driven  
 100 by diurnal wind and pressure variations. The largest glitches reach amplitudes of  $1e^{-7}ms^{-1}$  and  
 101 more. We observe a few of these per sol, whilst for amplitudes of  $>1e^{-8}ms^{-1}$  we can observe already  
 102 hundreds per sol. Especially in the early evening, when the wind and pressure variations calmed, we  
 103 observe a period with many consecutive glitches mostly of lower amplitude. We illustrate this period  
 104 in Figure 2. Certain types of glitches can furthermore repeat over many consecutive sols and the  
 105 same local time, thus indicating a driving process behind their production. In the frequency domain,  
 106 glitches range from lowest frequencies up to almost 1 Hz, thus influencing analyses of seismic records,  
 107 especially for longer periods. If glitches can be modeled with a step in acceleration, which is the  
 108 working hypothesis of this study, then their spectrum is  $1/f$  multiplied by the instrument response.

## 109 Glitch Precursors

110 Many glitches, furthermore, show a high-frequency signal at the very glitch beginning which lasts  
 111  $\sim 2$  s. We refer to these initial oscillations as "glitch precursors". These precursors occur simulta-  
 112 neously with the glitch onset for both VBB and SP (Fig. 1b,d). Glitch precursors do not represent  
 113 artifacts caused by the on-board data decimation but instead, as we demonstrate, can be modeled as  
 114 a response to a step in displacement. To facilitate the analysis of glitches and help deciphering their  
 115 origins, we analyse these precursors as well.

## 116 2 Glitch Detection

117 To automatically detect glitches on SEIS' VBB and SP raw data, several groups (MPS, ISAE,  
 118 UCLA, IPGP) independently developed algorithms in the Python and MATLAB programming lan-  
 119 guages. We describe these approaches in the following. The common detection idea, and working  
 120 hypothesis of this study, is that glitches in the raw data represent steps in acceleration convolved with  
 121 the seismometer's instrument response. The lists of detected glitches for each method can be found  
 122 in the Supplementary Information 1.

### 123 2.1 Glitch Detection by Instrument Response Deconvolution (MPS)

124 This detection algorithm, implemented in Python (Rossum, 1995) and ObsPy (Krischer et al.,  
 125 2015; Beyreuther et al., 2010), performs the following processing steps on a given period of three-  
 126 component seismic data (components U, V, W): (i) ensure all three seismic channels are present  
 127 and cut to equal length, i.e. handle gaps and overlaps, (ii) decimate the data to two samples per  
 128 second (sps), allowing all data per seismometer to be run with the same parameters, (iii) deconvolve  
 129 the instrument response on each component and convert to acceleration, (iv) band-pass filter the  
 130 acceleration data (e.g. 10-1000 s, 0.001-0.1 Hz), so the steps in acceleration emerge more clearly,  
 131 (v) calculate the time derivative of the filtered acceleration data so the acceleration steps become  
 132 impulse-like signals, and (vi) trigger positive and negative glitches when the absolute value of the

133 third derivative exceeds a constant. To avoid triggering on subsequent samples also exceeding the  
 134 threshold but belonging to the same glitch, we introduce a window length in which no further glitch  
 135 can be triggered. This parameter can be thought of as *minimum glitch length*. We note this parameter  
 136 is smaller than the typical glitch length for VBB and SP, allowing our detection algorithm to detect  
 137 poly-glitches.

138 The above processing results in a list of glitch start times for each of the individual UVW-  
 139 components. A glitch simultaneously occurring on multiple components is detected on each affected  
 140 component but the respective start times may slightly differ. However, after modeling of the full  
 141 glitch waveform (Section 4) we can retrospectively establish that such glitches occur at the same time  
 142 to within milliseconds. This holds true for all multi-component glitches observed to date on either  
 143 VBB or SP, also for data with the highest available sampling frequency of 100 Hz. Therefore, we  
 144 unify the individual glitch start times across the UVW-components by searching for all glitch starts  
 145 within minimum glitch length and use the earliest as the actual glitch start time. This unified list of  
 146 glitch starts contains still many false-positive triggers that caused by non-glitches with a steep enough  
 147 acceleration change to be triggered. This is because we choose to apply a constant threshold to the  
 148 time derivative of the filtered acceleration, rather than a threshold based on the current seismic noise  
 149 level that undergoes glaring diurnal changes dominated by meteorological influences (e.g. Banfield  
 150 et al., 2020). Due to this constant threshold our algorithm falsely triggers on non-glitches especially  
 151 during the noisy daytime. To circumvent this we rotate the gain-corrected UVW raw data of the  
 152 glitch windows into the geographical reference frame (ZNE-components) and perform a 3-D principle  
 153 component analysis (e.g. Scholz et al., 2017). Theoretically a glitch to be linearly polarized as the  
 154 associated vector of acceleration change is not varying. This linear polarization can only be slightly  
 155 reduced by seismic noise. Indeed, we find most glitches exhibit a high linear polarization  $>0.9$ , a fact  
 156 that we use to discriminate against other triggered signals. The polarization analysis further allows  
 157 to obtain the apparent glitch azimuth and incidence angle which can be used to associate glitches  
 158 with a particular glitch source (Section 3). Visual inspection reveals the resulting glitch onsets are  
 159 usually accurate to within  $\pm 1$  s (e.g. green lines in Fig. 1b,d). We note that scheduled movements  
 160 of InSight’s robotic arm may be identified as glitches, however, these movement times are known and  
 161 occur during the Martian daytime when we detect relatively few glitches. At times we also detect  
 162 convective vortices (e.g. Banfield et al., 2020) as they can produce glitch-like signals in the seismic  
 163 data (Section 6.3).

## 164 2.2 Glitch Detection by Cross-Correlation with Impulse Response Function (ISAE)

165 The principle of this MATLAB-implemented detection algorithm is cross-correlation. It performs  
 166 the following processing steps on a given period of three-component raw seismic data (components  
 167 U, V, W for VBB, or 1, 2, 3 for SP in counts): (i) a synthetic glitch is constructed by convolving  
 168 the poles and zeros of the transfer function of the VBB and SP sensors with a step in acceleration.  
 169 To increase the temporal resolution to sub-sample range, we synthesise several glitches each with a  
 170 different sub-sample time shift, (ii) the long period variations of the data are extracted using 1000 s  
 171 low-pass filter for VBB and 4000 s low-pass filter for SP. These are then subtracted from the signal  
 172 (and be added back at the end), before (iii) the synthetic glitch is cross-correlated with the data. A  
 173 glitch detection is triggered for the maxima of the cross-correlation function that exceed a threshold  
 174  $a$  on a given component.

175 Another step is added to prevent non-detection of glitches or false-positives, depending on the  
 176 correlation threshold. For that, two thresholds are chosen: *threshold a* and *threshold b*, with  $a \geq$   
 177  $b$ . The first step presented above (cross-correlation) is done for each component, with *threshold a*.  
 178 Then, for each component, a second cross-correlation with *threshold b* is implemented. For the times  
 179 of every maximum of cross-correlation exceeding *threshold b*, we come back to the glitches detected  
 180 on the other components during the first step. If a glitch had indeed been detected at that specific  
 181 time on another component, a new glitch is declared on the component under study. We can therefore  
 182 detect small glitches, with low signal-to-noise ratio, when a strong glitch is detected at the same time  
 183 on some other component. In addition, in order to be able to detect poly-glitches, a second iteration  
 184 of the detection algorithm is performed after the glitches from the first iteration have been removed  
 185 from the data.

### 2.3 Hierarchical Glitch Detection (UCLA)

This MATLAB based method took into account that glitch amplitudes follow a power law distribution with many more very small glitches than larger ones. Therefore the strategy was to remove the largest glitches first and repeat the process on the smaller ones in an iterative procedure. In this method the raw UVW VEL channel data are inspected for glitches and their precursors. The instrument response to a step in acceleration was termed "Green's function." The 20 sps data were decimated to 2 sps and each channel was tested for correlation with the response function as follows. An inverse filter was designed that turned glitches into Gaussians so that each glitch represented one peak without the overshoot. An STA/LTA ratio was found using convolution of the data with box car functions. The absolute value of band-passed data was tested for peaks above the STA/LTA threshold. For the first iteration the STA/LTA (short time average / long time average) was set large to remove the largest glitches. The Green function was correlated with the data spanning a peak and if the correlation coefficient was above 0.95 the detection was registered. If multiple peaks occurred close together multiple Green functions were fit to the data using nonlinear least squares. The data was then cleaned by removing the glitches. The process was then repeated lowering the STA/LTA threshold=7, and the new glitches removed from the data. For the last iteration the STA/LTA threshold was set to 3 i.e., lowered again and the correlation threshold was also lowered to 0.8. This removed many of the small glitches. Our glitch detection is applicable to SEIS' VBB and SP sensors in both low and high gain modes.

### 2.4 Triple-Source based Glitch Detection (IPGP)

Implemented in MATLAB, this glitch detection method processes mostly 2 sps continuous data and is therefore focused on long period continuous signals. It first removes the aseismic signals of each raw axis by subtracting the trend and the first 12 sol-harmonics (i.e., up to 1/12 sol period, about 0.13 mHz in frequency). Then the three axes are equalized in digital units by convolving the V and W channels by the convolution ratio of the U/V and U/W transfer functions, in order to correct for the gain and transfer function differences between U, V and W. Note that this process also transforms an impulse response in time on V and W into an impulse response with the U transfer function. As the inversion (below) is a linear one, the glitch search and deglitching can then be done either on the U, V-corrected and W-corrected channels or on the Z, N, E rotated channels, with practically no differences for the inverted glitches, although the variances are of course different on U, V, W and Z, N, E.

The glitch detection is done first by identifying all extrema in the signal and then, for all found extrema, least-square testing for the occurrence of a glitch using a modeled glitch. To model a glitch, we convolve a step in acceleration not only for one sample (as all other methods) but for three consecutive samples. As we have equalized all components beforehand, we only use the poles and zeros of the U-component for this step. Continuity of the signal is forced at the beginning and at the end of the glitch window by Lagrangian multipliers (Lagrange, 1813). The signal is then considered a glitch when the variance residual after glitch removal is less than 1–2 % of the original data squared energy over a running window of 50 s, starting 5 s before the glitch center. After the glitch removal, a delta impulse is then searched around the glitch time and removed if associated with a 50 % variance reduction of the signal in a window of width  $\pm 3$  s. Glitches and precursor amplitudes are inverted on the three axes. We use these amplitudes to calculate dip, azimuth and amplitudes of the precursors that we use to potentially located glitch source (Section 6.1). An average of about 170 glitches per sol is found for 1 % of variance residual and about 100 glitches per sol for 0.5 % of variance residual. For the former case, about 40 % are detected on the three components while the other are on single VBB components. As this approach is detecting the glitch through the success of the functions' fit with data, glitch removal is a sub-product of the method.

### 2.5 Performance of Glitch Detection Algorithms

A 24 hours comparison of our glitch detection algorithms is illustrated Figure 2. The detection threshold for some methods was set low in order to examine differences in the detections close to the ambient seismic noise levels. For example, ISAE and UCLA used a correlation coefficient threshold of 0.8 which opens the possibility that some of the detections may be noise. Approximately 250 detections were made by UCLA and IPGP, and 140 by MPS and ISAE, however, the latter two detected less

239 glitches during the noise daytime. Figure 2a shows the 73 glitches that were common to all 4 groups,  
 240 which correspond to those with the largest amplitude. Table 1 shows the number of detected glitches  
 241 common to pairs of groups. The non-common glitches are plotted color-coded according to each  
 242 group. A zoomed-in section (Fig. 2b) reveals that the various criteria detect mutually exclusive  
 243 glitches as the noise level is approached. We note that the MarsQuakeService (MQS, Clinton et al.,  
 244 2018) continuously monitors InSight’s seismic data to detect and catalogue seismic events (InSight  
 245 Marsquake Service, 2020). As part of their routine they manually seek and annotate glitches with  
 246 principal focus on time windows of seismic events. Our detection methods generally compare well  
 247 with these manual annotations both in amount and onsets of glitches, especially for larger ones.

**Table 1.** Common glitch detections between group pairs for July 1 2019, sol 211. Based on data of 02.BHV (VBB at 20 sps). Note that all algorithms equally detect the largest 73 glitches.

<b>GROUP</b>	<b>MPS</b>	<b>ISAE</b>	<b>IPGP</b>
<b>ISAE</b>	94		
<b>IPGP</b>	102	95	
<b>UCLA</b>	105	100	121

### 248 3 Glitch Analysis

249 Our working hypothesis is that glitches in SEIS’ time series data represent sudden steps in the  
 250 sensed acceleration convolved with the instrument response of the respective seismometer, either VBB  
 251 or SP. We can use that assumption to constrain the physical mechanism that led to the glitch. When  
 252 interpreted as an inertial acceleration  $\ddot{x}(t)$  of the seismometer frame, a step in acceleration translates  
 253 to a unlimited linear increase of velocity. This of course becomes quickly non-physical and can be  
 254 ruled out because it implied that SEIS by now would have left its landing location. On the other hand,  
 255 accelerometers like the VBB or SP are also sensitive to changes in gravity. One way this can occur  
 256 is by tilting the instrument, thus causing a change of projection of the local gravity vector onto the  
 257 directions of the sensitive sensor axes. For small tilt angles  $\alpha$ , this translates into a first order effect  
 258 for the horizontal components ( $\sim \sin(\alpha) \approx \alpha$ ) but only a second order effect for the vertical component  
 259 ( $\sim [1 - \cos(\alpha)] \approx \alpha^2/2$ ). The vector sum of acceleration changes in U, V and W due to a tilt of the  
 260 SEIS sensor assembly (including the leveling system) must therefore point in the horizontal direction.  
 261 This is true for both SP and VBB. Any other direction cannot be explained by a rigid motion of  
 262 SEIS and must be due to instrumental artifacts. These can be internal tilt of one VBB sensor with  
 263 respect to the others, spring relaxation of any sensor, or even offsets in the electrical voltage of the  
 264 displacement transducers which cannot be distinguished from mechanical offsets of the latter.

265 It is useful at this point to recall the sign convention for accelerometers: a positive output signal  
 266 corresponds to a positive acceleration of the frame in the sensitive direction, not the direction in which  
 267 the proof mass moved. The proof mass – due to its inertia – lags behind the motion of the frame. It  
 268 follows that if one analyses the apparent glitch azimuth and incidence angles under consideration of  
 269 the actual sensor orientations and arguments above, as well as the behaviour of these angles over time,  
 270 one can draw conclusions on possible glitch origins. The analysis of apparent glitch polarizations is  
 271 therefore our method of choice.

272 The determination of the apparent glitch azimuth and incidence angles is implemented in our  
 273 glitch detection algorithm (Section 2.1). As described, once a glitch onset is detected, the algorithm  
 274 uses the raw data of the three components of the seismometer the glitch occurred on (either VBB  
 275 or SP), divides by the respective sensor gains, rotates the data into the geographical reference frame  
 276 (ZNE-components) and performs a 3-D principle component analysis (e.g. Scholz et al., 2017). To  
 277 resolve the  $180^\circ$  ambiguity inherent to that method, we used the fact that glitches have a clear  
 278 one-sided pulse (1b,d); a glitch of positive polarity on the N-component is associated with a step in  
 279 acceleration acting in this direction, its respective azimuth is therefore  $\approx 0^\circ$  (assuming there is no glitch  
 280 on the E-component). The same consideration holds true for a glitch showing on the (reconstructed)  
 281 vertical component.

Based on our glitch detection algorithm presented in Section 2.1, Figures 3–5 demonstrate the polarization analysis of the VBB and SP glitches. The plots incorporate two VBB channels 02.BH? and 03.BH? (20 sps and 10 sps, respectively), and two SP channels 67.SH? and 68.SH? (20 sps and 10 sps sample rate, respectively). These are the channels that, depending on the actual satellite down-link capacities, are continuously returned to earth. For more detailed information on available SEIS channels, see Lognonné et al. (2019). Besides some minor data gaps in this continuous operation, there is a large period with no data return between sols 267–288. This is due to the solar conjunction period where Earth-Mars communications were obscured by the sun as consequence of their relative orbital positions. With respect to the Local Mean Solar Time (LMST, local InSight time, e.g. Allison & McEwen, 2000), the polarization patterns prevail over many sols and we discuss some of them in the following to understand the glitch behaviour in more detail. First, we demonstrate that our polarization analysis is correct and explain why the results are not intuitive for certain cases for VBB and SP. We then discuss glitches occurring on only one VBB or SP component before building our arguments for multi-component glitches. We conclude this section by looking at glitches that occurred simultaneously on VBB and SP. Note that all details concerning the SEIS sensor assembly can be found in Lognonné et al. (2019).

### 3.1 Theoretical Considerations for apparent Glitch Polarizations

The glitch polarization describes the direction (azimuth and inclination) in which the SEIS sensor assembly is accelerated in order to produce the observed glitch signal on the three sensors U, V and W of VBB and SP, respectively. Thus, irrespective of analyzing a one-component or a multi-component glitch, we map the non-orthogonal UVW-components (Fig 1ac) into the orthogonal ZNE-components before computing azimuth and inclination. For a one-component glitch the non-orthogonality of the VBB components leads to the non-intuitive result that the azimuth differs slightly from the azimuth of the affected sensor while the incidence angle of the same one-component glitch differs by  $\sim 12^\circ$  from the sensor's dip angle. We demonstrate this relation in the following.

Projecting the seismometer components from the orthogonal basis vectors Z (positive up), N (positive North), and E (positive East) onto the arbitrarily oriented basis of UVW, we must start with the following linear system of equations:

$$\begin{pmatrix} U \\ V \\ W \end{pmatrix} = \underbrace{\begin{pmatrix} -\sin(\delta_U) & \cos(\delta_U) \cos(\phi_U) & \cos(\delta_U) \sin(\phi_U) \\ -\sin(\delta_V) & \cos(\delta_V) \cos(\phi_V) & \cos(\delta_V) \sin(\phi_V) \\ -\sin(\delta_W) & \cos(\delta_W) \cos(\phi_W) & \cos(\delta_W) \sin(\phi_W) \end{pmatrix}}_A \cdot \begin{pmatrix} Z \\ N \\ E \end{pmatrix}, \quad (1)$$

where  $A$  represents the base transformation matrix,  $\delta_i$  the sensor dip of sensor  $i$ , and  $\phi_i$  the sensor azimuth of sensor  $i$  clockwise from N. Note that sensor dipo are defined as positive downwards from the horizontal plane (e.g. Ahern et al., 2012). To reconstruct data recorded in the UVW-system into the ZNE-system, we must use the inverse operation:

$$\begin{pmatrix} Z \\ N \\ E \end{pmatrix} = A^{-1} \cdot \begin{pmatrix} U \\ V \\ W \end{pmatrix}, \quad (2)$$

with  $A^{-1}$  the inverse matrix of  $A$ . If we now consider a glitch that occurred only on VBB U with an amplitude  $U = 1$  ( $V = 0, W = 0$ ), insert those values into Equation 2, and use the following equations to determine the apparent glitch azimuth defined clock-wise from N,  $AZ$ , and apparent glitch incidence defined from Z,  $INC$ , it follows:

$$\begin{aligned} AZ &= \text{atan2}(E, N) = \text{atan2}(A_{31}^{-1}, A_{21}^{-1}) \\ INC &= \text{acos} \left( \frac{\langle [Z, 0, 0]^T, [Z, N, E]^T \rangle}{\| [Z, 0, 0]^T \| \cdot \| [Z, N, E]^T \|} \right) = \text{acos} \left( \frac{A_{11}^{-1}}{\sqrt{(A_{11}^{-1})^2 + (A_{21}^{-1})^2 + (A_{31}^{-1})^2}} \right). \end{aligned} \quad (3)$$

318 We can calculate the inverse matrix elements  $A_{j1}^{-1}$  with the known VBB U sensor azimuth and dip  
 319  $\phi_U = 135.1^\circ$  and  $\delta_U = -29.7^\circ$ , respectively, and find:

$$\begin{aligned} AZ &= 134.6^\circ \neq 135.1^\circ = \phi_U \\ INC &= 48.5^\circ \neq 60.3^\circ = 90.0^\circ + \delta_U. \end{aligned} \quad (4)$$

320 Therefore, the apparent azimuth and incidence angles of a one-component VBB glitch will *not*  
 321 point in the direction parallel to the sensitive direction of the affected VBB sensor. Instead, the  
 322 vector spanned is parallel to the vector cross-product of the remaining two components that do not  
 323 show the glitch. Due to the similar arrangement of all VBB's sensors, with azimuths of  $\phi_U = 135.1^\circ$ ,  
 324  $\phi_V = 15.0^\circ$  and  $\phi_W = 255.0^\circ$ , and dipo of  $\delta_U = -29.7^\circ$ ,  $\delta_V = -29.2^\circ$  and  $\delta_W = -29.4^\circ$  (see Fig. 1a),  
 325 the case demonstrated for VBB U holds true for VBB V and VBB W, too. Therefore for all VBB  
 326 components, a one-component glitch polarization analysis will deliver azimuth angles (almost) parallel  
 327 to the sensor azimuths and hence be intuitive, whilst incidence angles will be  $INC \sim 48^\circ/132^\circ$  as  
 328 opposed to the sensor incidences of  $90.0^\circ + \delta_i \approx 60^\circ$  (or  $120^\circ$ ). For multi-component VBB glitches  
 329 similar considerations disclose the calculated azimuths will also be intuitive, however, for a two-  
 330 component glitch the incidence must be  $INC \simeq 30.0^\circ\text{--}150^\circ$  (within a plane orthogonal to the third  
 331 component), whilst for a three-component glitch the incidence can range the whole parameter space  
 332 of  $INC = 0^\circ\text{--}180^\circ$ . It follows immediately that any VBB glitch for which we observe an  $INC < 30^\circ$   
 333 or  $INC > 150^\circ$  must, necessarily, affect all three VBB components.

334 Doing the same exercise for SP, with azimuths of  $\phi_U = 285.0^\circ$ ,  $\phi_V = 105.2^\circ$  and  $\phi_W = 345.3^\circ$ ,  
 335 and dipo of  $\delta_U = -89.9^\circ$ ,  $\delta_V = 0.0^\circ$  and  $\delta_W = 0.0^\circ$  (see Fig. 1c), one finds that for SP U (Z)  
 336 the azimuth and incidence angles will follow one's intuition closely and be  $0^\circ$  and  $0^\circ$ , respectively.  
 337 For the horizontal components SP V and SP W the case is different: a SP V glitch will reveal an  
 338 incidence angle of  $INC = 89.9^\circ\text{--}90.1^\circ$  as expected, but an azimuth of  $AZ \sim 075^\circ/255^\circ$ , which is  
 339 not intuitive given its sensor azimuth of  $\phi_V = 105.2^\circ$ . Similarly for SP W, the incidence angle  
 340 will be  $INC = 89.9^\circ\text{--}90.1^\circ$  but the azimuth  $AZ \sim 015^\circ/195^\circ$ , as opposed to the sensor azimuth of  
 341  $\phi_W = 345.2^\circ$ . A direct consequence is that any SP glitch pointing parallel to the SP V or SP W  
 342 sensor azimuths must be in fact a multi-component SP glitch. For multi-component SP glitches, we  
 343 did not detect any glitches that occur on the vertical SP U component in combination with either one  
 344 or two of the horizontal components SP V and SP W. That is, the only multi-component SP glitches  
 345 are two-component glitches on SP V and SP W. Multi-component SP glitches are therefore always  
 346 oriented in the horizontal plane.

347 The message from these theoretical considerations is that our glitch polarization analysis will  
 348 deliver azimuths and incidence angles that correctly incorporate the non-orthogonality of VBB and  
 349 SP; the vectors spanned by these angles point into the only physically possible directions for a given  
 350 one-, two- or three-component glitch. On the other hand, for the interpretations of these angles, it  
 351 must be born in mind that VBB incidence angles may carry counter-intuitive information, whilst  
 352 SP azimuth angles for one-component glitches will not align with the respective sensor azimuths but  
 353 diverge by  $\sim 30^\circ$ . We have started this section by stating that the glitch polarisation points in the  
 354 direction in which SEIS has to be accelerated in order to produce the observed output. However, for  
 355 glitches which are not associated with an acceleration of the entire sensor assembly (i.e. no tilt of the  
 356 whole SEIS instrument) the adopted convention needs to be used with caution - particularly given  
 357 the non-orthogonality of the sensors. Still we feel that the concept of glitch polarization is useful.

358 At this stage we also note that whilst the poles and zeros of the seismometer responses are well  
 359 determined, the same does not apply fully for the generator constants (gains). In the worst case they  
 360 may differ up to 10% from the absolute values known by pre-mission tests. To convince ourselves  
 361 of the correctness of determined glitch azimuths and incidences with respect to these constants we  
 362 conducted a test: we took the raw data of one- and multi-component glitches of different amplitudes  
 363 and divided the respective components by their gains that we allowed to vary each by up to  $\pm 10\%$ .  
 364 For each permutation, we then rotated into the ZNE-system and performed the polarization analysis.  
 365 For VBB, we find that glitch azimuths and incidences generally stay within  $\pm 5^\circ$  and  $\pm 4^\circ$ , respectively.  
 366 For SP, we find that glitch azimuths and incidences generally stay within  $\pm 3^\circ$  and  $\pm 1^\circ$ , respectively,  
 367 the latter of which is because SP multi-component glitches occur only on the horizontal components.  
 368 All these values are smaller than the typical errors of polarization measurements and we can therefore  
 369 assume the resulting glitch patterns to be reliable.

### 3.2 Glitches on only one seismometer component

For VBB, amplitudes of one-component glitches are usually  $<1e^{-7}ms^{-1}$  and are thus not amongst the largest ones observed. Furthermore, a glitch occurring on only one single component cannot be interpreted as the SEIS instrument tilting. Such a glitch would necessarily have an incidence angle of  $INC \sim 48^\circ/132^\circ$  (see Section 3.1) whilst the only possible direction of acceleration change would point (nearly) in the horizontal plane for a true SEIS tilt. We hence conclude that a VBB one-component glitch can only be related to instrumental artifacts such as (but not limited to) thermally driven stress relaxations in the suspension spring or pivot, displacement of one of the fixed plates of the displacement transducer, voltage offsets in the individual feedback electronics, or tilting of the individual sensor within the SEIS frame. Figure 3a,b shows the VBB one-component glitches. For most identifiable patterns we find their behaviour clearly changed either when the SEIS heaters were turned on (these are mounted on the leveling ring, see Lognonné et al., 2019) on sol 168 (2019-05-19), or after the solar conjunction period in which the heaters were off and the SEIS instrument cooled down. This plus the fact these glitch patterns emerge due to their recurrence with respect to the local time, i.e. repetitively at the same time of the sol, leads us to conclude that they are indeed thermally driven. What we suspect is that the enormous Martian surface temperature changes, that can reach up  $100^\circ C$  each sol, introduce stresses into the material – possibly within the Evacuated Container (EC, "sphere"). Even though the temperatures inside SEIS do not vary as much as outside, the stresses grow and are released once at a critical temperature is reached, thereby producing a glitch. When the heaters are on, the SEIS' thermal regime exhibits essentially higher temperatures and, in second order, lower diurnal amplitudes and thermal spatial gradients. This contributes to minimize thermal stresses in this complex assembly, thus diminishing or at least altering glitch production. We demonstrate heater-related glitch behaviour in more detail in the next section for multi-component glitches. We have no good explanation why we observe so many more glitches on VBB W compared to the other two VBB components, especially after the conjunction period during which the SEIS heater were off. Only after  $\sim 100$  sols the number of one-component glitches (mostly constitutes by glitches on VBB W) return to the pre-conjunction level (Fig. 3b).

For SP, a glitch occurring on only one single component could potentially be interpreted as the SEIS instrument tilting if the glitch shows one of the two horizontal components, SP V (2) or SP W (3). The tilt direction must furthermore be orthogonal to the other horizontal component so the glitch could only be seen on one component. More plausible than being caused by SEIS tilt we think is that these glitches are also thermally driven. Figure 3c demonstrates that the horizontal one-component SP glitches change their behaviour / occurrence with heater activation. For SP U, oriented almost vertically, a one-component glitch cannot be explained by instrument tilt because it does not point in the horizontal plane. These glitches therefore must relate to effects on the sensor level. Interestingly, Figure 3d demonstrates that SP U glitches that occur during the morning hours, i.e. when the environment becomes warmer, point upwards whilst during the evening/night hours, i.e. during the cooling cycle, the glitches point downwards. We interpret this behaviour as further evidence for the thermally driven nature of one-component glitches. Glitches occurring on the SP U and on the (reconstructed) VBB Z in contrast support a non-mechanical origin, possibly related to voltage offsets on the displacement transducers lines.

### 3.3 Glitches on multiple seismometer components

The multi-component glitches for VBB and SP are illustrated in Figure 4. Especially for VBB, for which we generally detect more glitches, clear patterns emerge over the period of 2019. We discuss five of these patterns in the following.

We observe a clear glitch pattern with associated acceleration change pointing towards North (blue dots, pattern 1). These three-component glitches are often accompanied by glitch precursors and occur around 1800 LMST and thus when the local temperatures start dropping. The incidence angles are  $\sim 90^\circ$  (in the horizontal plane) and hence may represent the SEIS instrument tilting. For this glitch pattern, however, we observe an additional 4.2 Hz ringing in some cases for the duration of the glitch, something not expected for an unhindered SEIS tilt. This occasional ringing could be related to other short duration data artefacts we observe mostly in data with higher sampling frequencies ( $>20$  sps). We termed these data artifacts "donks" and they are still under investigation. Therefore for the glitches of pattern 1, we currently favour the possibility that they are produced

424 due to the temperature decrease of the tether and/or Load Shunt Assembly (LSA), both located at  
 425 azimuths  $\sim 15^\circ$  and connecting SEIS with the InSight lander, contract and produce these glitches.  
 426 This argument is supported by the fact that the heater activation on sol 168 (2019-05-19) seemed to  
 427 have no significant effect on these glitches (Fig. 4c), bearing in mind that the heaters are located  
 428 within SEIS and the LSA/tether is not. Furthermore, the largest of these VBB glitches (amplitudes  
 429 larger than  $1e^{-7}ms^{-1}$ ) are also observed on SP with agreeing glitch azimuths and incidence angles  
 430 (Fig. 5), and the same 4.2 Hz ringing. It therefore could be concluded that this glitch pattern is  
 431 indeed due the SEIS instrument tilting, caused by cooling effects of the tether and/or LSA that also  
 432 cause the 4.2 Hz ringing. On the other hand, the glitch azimuths of pattern 1 average to  $\sim 0^\circ$  and not  
 433  $\sim 15^\circ$  where the LSA/tether are located. Furthermore, the acceleration changes associated with these  
 434 glitches point northward and hence suggest SEIS tilting southward, something difficult to reconcile  
 435 with e.g. the contracting tether "pulling" SEIS. One may therefore suspect not the tether itself as  
 436 possible glitch cause but instead its connection with SEIS. Interestingly, there is another glitch pattern  
 437 (green dots, pattern 2) with similar features: azimuths pointing consistently south (instead of north),  
 438 incidence angles are  $\sim 90^\circ$ , often preceding glitch precursors, occurrence  $\sim 1000$  LMST (instead of  
 439 1800), occasional 4.2 Hz ringing during the glitch, no significant effect of heater activation on glitch  
 440 amount, and the largest amongst them also visible on SP with coinciding azimuths and incidence  
 441 angles (Fig. 5). This pattern could represent the counter-part to pattern 1; in the warming cycle of  
 442 the day the glitch cause reverses.

443 The glitches with azimuths  $\sim 240^\circ$  occurring around 2100 LMST (pink dots, pattern 3) show  
 444 clear indications of being thermally driven. These three-component glitches with accompanying glitch  
 445 precursors, that are not seen on SP, appear just after SEIS heater activation whilst before they were  
 446 absent. Their consistent incidence angles of  $\sim 100^\circ$  prohibit their interpretation of SEIS tilting but  
 447 instead point towards a thermal effect acting on all VBB sensors. After the conjunction period, during  
 448 which the heaters were off, they do not immediately reappear with the heater re-activation but only  
 449  $\sim 30$  sols later together with azimuths being more variable. We noted such conjunction-delayed be-  
 450 haviour (before the pre-conjunction state is reached again) already for VBB's one-component glitches  
 451 (Fig. 3a,b). However, it is also readily visible for other multi-component patterns during the night  
 452 time (red and pinks dots at azimuths of  $\sim 40^\circ$ ). For these reasons, such glitch patterns are likely to  
 453 represent SEIS-internal, thermal effects. This is further supported by the glitch histogram in Figure  
 454 4e that clearly shows reduced glitches for the night time (many fewer red dots) just after heater ac-  
 455 tivation. We note that there is a similar pattern on SP at azimuths of  $\sim 350^\circ$  (red dots) that occurs  
 456 at the same times as the corresponding VBB one.

457 Another prominent VBB multi-component glitch pattern occurs in the early sol-hours with az-  
 458 imuths mostly due East (yellow to orange dots, pattern 4). These three-component glitches with  
 459 accompanying glitch precursors, that are not seen on SP, happen during the diurnal cooling cycle.  
 460 Although there seems to be no obvious influence by the heater activation (or re-activation after con-  
 461 junction), with increasing sols they occur at earlier hours. This plus the fact that their incidence  
 462 angles exclude a rigid tilt of the SEIS instrument lets us conclude that for this group, too, thermal  
 463 effects are the primary glitch cause.

464 There is another thermally-driven glitch pattern that appears on both VBB and SP in the early  
 465 morning (yellow-orange-red dots, pattern 5), which again leads to glitches on the vertical VBB com-  
 466 ponent. It is discussed in detail in the next Section 3.4.

467 Patterns 3, 4 and 5 are therefore all associated with non-horizontal incidence angles suggesting  
 468 that the three VBB sensors are not detecting an overall instrument tilt. Instead, each of the three  
 469 VBBs detects a different tilt that consequently leads to the non-zero glitch on the vertical axis. The  
 470 VBB sensors are mounted on a titanium plate inside the Evacuated Container (EC) through three  
 471 mounting bolts oriented at azimuths of  $105^\circ$  (IF1),  $225^\circ$  (IF2) and  $345^\circ$  (IF3). So, the first one is  
 472 pointing roughly due east, while the two other ones point due west and are symmetrically to one  
 473 another with respect to the West. This configuration produces colder temperatures on the east side  
 474 during the night than on the west side (and the opposite during the day), with larger gradients between  
 475 IF1-IF2 or IF1-IF3 than between IF2-IF3. This is likely the primary source of these thermal glitch  
 476 patterns. We note that the temperatures between the inside and outside of the EC are out of phase  
 477 with the outside being ahead by about 7-9 hours (Pou et al., 2019).

### 3.4 Glitches on both VBB and SP

Figure 5 shows all glitches that occurred within  $\pm 2$  seconds on both VBB and SP. From these 638 glitches, 118 glitches reveal the same azimuths to within  $\pm 10^\circ$ . Most of the glitches on VBB and SP that match in azimuth were discussed already in the previous Section 3.3 (green and blue dots, parts of patterns 1 and 2). As we pointed out, these glitches show incidence angles of  $\sim 90^\circ$  for both VBB and SP and therefore could signify the whole SEIS instrument tilting.

The most prominent glitch pattern in Figure 5 is the one at azimuths of  $\sim 145^\circ$  for VBB and  $\sim 110^\circ$  for SP (yellow-orange-red dots, pattern 5). From the beginning of SEIS' operational mode, these relatively strong glitches occurred once every morning with persistent glitch azimuths throughout 2019. Between sols 80–167, so before SEIS' heater activation, their onset times shift each sol by on average 4 Martian minutes ( $\sim 2\%$  longer than SI minutes). This can be interpreted as the glitches occurring at a critical temperature during the cooling cycle that is reached earlier every sol as the Northern hemisphere (where InSight is) is entering the colder season. When the heaters were turned on, leading to SEIS being in a thermally mitigated state, the glitches continued drifting towards earlier times but now with an average rate of less than 2 minutes per sol. After the conjunction period, during which the heaters were turned off, we observe the same as for many other glitch patterns; a more diffuse signature of the glitch azimuths and incidence angles that seem to return to pre-conjunction states only  $\sim 100$  sols later. Also, the onsets time now drift towards later times (red to yellow) each sol which interestingly coincides with the fact that the Martian solstice occurred just after the conjunction on sol 308. For this pattern as a whole, we were able to clearly identify the critical temperature around which the glitches occur. As Figure 4d,f demonstrates, the glitch onset times strikingly follow the iso-temperature curve at  $-54^\circ\text{C}$  for both VBB and SP. In addition for VBB, there are more patterns with similar behaviour for which we could find the critical temperatures; these correspond to pattern 3 (red and pink dots, Section 3.3). All this evidence once more supports the fact that most glitches are thermally caused. Note that the temperature sensor we used here is scientific temperature sensor A (SCIT A, channel 03.VKI), located at the northern, inner side of leveling support structure. The temperatures measured at this sensor can also occur elsewhere in the SEIS assembly at the same time.

## 4 Glitch Removal

Once a glitch, and its precursor if present, have been detected the waveforms are modeled as a linear combination of three constituents: (1) the glitch: the response of the seismometer to a step in acceleration, (2) the precursor: the response of the seismometer to a step in displacement and (3) the background drift: a first or second order polynomial. The two responses can be modeled from the pole and zero of their transfer function. Only the amplitudes and the precise timing of the source (which might be between two recorded samples) are to be inverted with such model.

The MPS group models a glitch waveform for each detected glitch using three parameters: an amplitude scaling factor, an offset, and a linear trend parameter. To find the best fit within a respective glitch time window, the model is iterated over each sample (no sub-sample implementation) and the best fit for the three parameters is determined. The deglitched data then is obtained by subtracting the fitted glitch without the offset and linear trend parameters from the original data. To prevent our method from removing data where the fit is not good enough, i.e. the model is fitted to data that are in fact not glitches or fitted to glitches that cannot fully be represented by our model of a step in acceleration, we correct glitches only for which we can achieve a variance reduction of  $> 85\%$  with respect to the overall glitch window. We find this threshold to generally permit the removal of all large glitches whilst small glitches are also removed if their waveforms represent that of the underlying model well. This method delivers comparable results for all sampling frequencies. An example of this glitch removal is shown in Figure 6.

Two groups (ISAE and UCLA) have been carrying out glitch removal on 10/20 sps data with the UCLA group adding precursor removal, which is the approach we describe here. Glitch and precursor templates were fit to the glitches and precursors, respectively, using non-linear least squares (NLSQ). Because of the delta-like shape of the precursor over one or two sample intervals, the starting model must find the location to within a fraction of a sample interval (0.05 s). Glitches are easier to fit than precursors, being low frequency, and requirements on the starting model are less stringent. Precursors

531 are much smaller in 2 sps data relative to glitch sizes. Thus 2 sps data were used to generate a glitch  
532 catalog (see Section 2).

533 The starting parameters from the 2 sps fits were then used to fit glitches in the 20 sps data  
534 and residuals were calculated. The residuals were examined for the presence of a precursor in the  
535 data before the glitch peak, by requiring its amplitude to be greater than 5 standard deviations of  
536 the residuals after the peak. If true, an iterative forward model was run by shifting the phase of the  
537 precursor template about the corresponding peak in the residuals (in steps of sample interval/10), and  
538 finding the amplitude and phase of maximum cross correlation. The NLSQ was run again with both  
539 precursor and glitch templates, and the result checked whether cross-correlation of data and model  
540 are above a threshold, and if so, the results are stored. At this stage, for poly-glitches (one on top of  
541 another) we search for the precursor at the beginning of the sequence. This may need to be improved  
542 in future versions. Even though a number of precursors have been removed, there are residuals and  
543 transients that remain.

544 Figure 7a shows an example for glitch removal (ISAE) and glitch plus precursor removal (UCLA)  
545 from the VBB W channel for sol 211. Atmospheric pressure effects, most notably convective vortices  
546 (Section 6.3), can also introduce signals in the seismic data. We find that transients in the time-  
547 derivative of the pressure channel (03.BDO) match, at times, closely with the glitch template. Using  
548 the largest of these examples, we determined a transfer function,  $T$ , between the data of VBB and  
549  $P$ . This allowed us via correlation analysis to detect whether the glitch-like signal on seismic data is  
550 caused by pressure effects and thus should not be removed by deglitching from the data.

551 The IGP group inverts three consecutive sources for the glitch which allows not only to invert  
552 for multi-component glitches occurring within these 3 samples but also to invert for the phase delay  
553 through finite-difference approximation of the first and second time derivative. This linear approach  
554 allows the inversion to provide identical results in the U, V, W coordinates or in the Z, N, E coordinates,  
555 as the rotation between the two coordinates systems is a linear relation. Conversely, the three other  
556 methods, through their non-linear part of the inversion or through the cross-correlation phase fitting,  
557 have built-in small reasons to provide different solutions depending on the coordinate systems. A  
558 comparison of spectrograms before and after deglitching using this method is shown in Figure 7b,c.

559 In the end, all the proposed deglitching methods are nevertheless based on the same impulse  
560 response model and mostly differ by their threshold below which a glitch is removed or not. No  
561 general rule on that threshold can be provided, as it depends on the data processing target. As an  
562 example, the three methods assuming strictly a single glitch (MPS, ISAE, UCLA) and the three-point  
563 source method (IPGP) provide similar deglitching for the large glitches occurring during the cooling  
564 periods and during the night. More freedom is available for fitting longer source duration glitches  
565 during the day by the three-point sources technique, although some of the latter may represent the  
566 real response of SEIS to a small pressure drop (see Section 6.3) which can generate nano-tilts. At  
567 the same time, while many precursors are fitted by the templates, there are a significant number that  
568 have quite different morphology, longer ringing, or longer-period transient behavior. These are the  
569 subject of ongoing work.

570 We also point out that we have discontinued our deglitching efforts using the stationary wavelet  
571 transform as described in the Supplement V of Lognonné et al. (2020). Whilst this approach provided  
572 promising and correct results for a fair amount of cases (as far as one can tell), there is no underlying,  
573 physical model involved and the implicit data 'correction' therefore seemed too arbitrary. For many  
574 cases this approach further introduced DC-offsets in the deglitched data whose amplitudes and lengths  
575 depended on the length of data read (and therefore maximum decomposition level); an artifact that  
576 we could never manage to fully avoid.

## 577 5 Glitch Model

578 Throughout this paper we have assumed that glitches can be understood as steps in acceleration  
579 and glitch precursors as steps in displacement. This model allowed us to successfully detect, analyse  
580 and remove one- and multi-component glitches for both VBB and SP. In the following we detail the  
581 theoretical considerations behind this simplified model.

582 Let us assume glitches are caused by a small instantaneous tilt. By instantaneous we mean that  
 583 the time history of the tilting is so short that it cannot be resolved with any given sampling frequency  
 584 available to us (maximum 100 sps). We are thus allowed to idealize any step in time by a Heaviside  
 585 function. Physically such short instantaneous events can for example be the result of stick-slip events.

586 The small tilt is assumed to be the result of a rotation around a horizontal axis,  $\vec{a}$ . Recall that  
 587 the VBB is a pendulum seismometer where the (inverted) pendulum is constrained to rotate around  
 588 a horizontal axis,  $\vec{b}$ . The sensitive direction,  $\vec{s}$ , of the pendulum is perpendicular to the  $\vec{b}$  axis and is  
 589 inclined relative to the horizontal plane by a dip angle of  $\delta = -29.3^\circ$ . Let us also assume for simplicity  
 590 that all the mass of the pendulum is concentrated in its center of gravity (CoG) - which would be the  
 591 case for a mathematical pendulum.

592 Now we can distinguish five cases which differ by the location of the accelerometer relative to the  
 593 tilt axis,  $\vec{a}$ :

594 (1) the two axes  $\vec{a}$  and  $\vec{b}$  are parallel and  $\vec{a}$  passes through CoG: in this case the accelerometer  
 595 gets only reoriented relative to the gravity vector but the CoG stays in place.

596 (2) the two axes are parallel and  $\vec{a}$  does not pass through CoG but is at the same height as the  
 597 CoG: in this case the accelerometer gets displaced vertically and reoriented relative to the gravity  
 598 vector. However this reorientation is negligible because it is only a second order effect.

599 (3) the two axes are parallel and  $\vec{a}$  does not pass through CoG. Furthermore a line parallel to  
 600  $\vec{s}$  passing through CG intersects with  $\vec{a}$ . In this case the accelerometer gets displaced vertically and  
 601 reoriented. However the displacement is in the direction perpendicular to the sensitive axis and hence  
 602 is not seen by the accelerometer. Only the reorientation is sensed.

603 (4) For all other locations of the rotation axis  $\vec{a}$  for which  $\vec{a}$  and  $\vec{b}$  are parallel the accelerometer  
 604 will see both a displacement and a reorientation relative to the gravity vector.

605 (5) For the general case where  $\vec{a}$  and  $\vec{b}$  are not parallel the same arguments can be made but the  
 606 effect sensed for a given tilt angle will always be reduced relative to the case with parallel axes  $\vec{a}$  and  
 607  $\vec{b}$  since the tilting is reduced.

608 As soon as the accelerometer gets reoriented relative to the gravity vector we expect to see the  
 609 response due to a step in acceleration, because the projection of the gravity vector into the sensitive  
 610 direction is changed. In those cases where the accelerometer gets displaced we expect to see the  
 611 response due to a step in displacement. The five cases then only differ in the relative size of the  
 612 displacement and tilting.

613 What do these signals look like? In Figure 6 we have plotted the response of the VBB sensors to  
 614 a step in acceleration and the response to a step in displacement (red lines). To model the instrument  
 615 response we take the full seed response and evaluate it with *evalresp* - a piece of software provided  
 616 by the IRIS/DMC. Figure 6 also demonstrates how we can use the modelled glitch and precursors to  
 617 remove them from the data.

618 Can these signals explain the data? As Figure 6 also demonstrates, the modeled responses have  
 619 been shifted in time and scaled to match the data. The fit is excellent both for the low-frequency  
 620 glitch and the high-frequency precursor. We take this as confirmation that our simple model is  
 621 capable of explaining the glitch waveform with four parameters: start-time and amplitude of the step  
 622 in acceleration plus the start-time and amplitude of the step in displacement. In fact we could show  
 623 that the start times of the acceleration and displacement steps coincide to the millisecond - which is  
 624 what our model predicts. Thus we only need three parameters: the start time and the amplitudes  
 625 in displacement and acceleration. Determining the start time requires an excellent calibration of the  
 626 high frequency part of the sensors transfer functions, as well as high sampling rate. While deglitching  
 627 on the 20 sps data is therefore much more precise and has been done for two of the described methods,  
 628 the deglitching on lower rate data, e.g. 10 sps (UCLA) or even 2 sps (IPGP) can be achieved, including  
 629 for the precursor amplitude, however, with the signal-to-noise ratio reduced by the frequency ratio of  
 630 the bandwidth. Fitting the precursor plus glitch with these three parameters implies determining the  
 631 start time to sub-sample resolution. We provide a more mathematical description of our model for  
 632 the glitch plus precursors phenomenon in the Supplementary Information 2.

## 6 Discussion

In the following we briefly discuss other aspects of glitches and precursors that we encountered during our investigations. This section shall therefore complement our understanding of glitches and detail some more implications.

### 6.1 Possibly locating SEIS-internal tilts

Our glitch model presented in Section 5 is valid for rotations of the sensor assembly as a whole (e.g. caused by a change at one foot of the sensor assembly), for just the VBB sensors (e.g. caused by stick-slip events originating at the sphere-ring interface, i.e. between the Evacuated Container and the leveling support structure), but also for an individual sensor (e.g. caused by stick-slip events originating at the sensor-support interface or at the fixed side of the pivot or spring). Each of these cases implies a different value of  $r$ : the distance between VBB U to the sensor assembly feet at 16 or 21 cm (Fayon et al., 2018), or the distance from the sensor’s center of gravity to its pivot with 2.6 cm (Lognonné et al., 2019).

We illustrate this geometry with the glitch example of Figure 6 and recall the glitch and precursor characteristics in Table 2. This glitch has a vertical component and can therefore not represent the SEIS instrument tilting as a whole. The azimuth of the glitch opposite (opposite of acceleration) and of the precursor (displacement) are  $219^\circ$  and  $228^\circ$ , respectively. These values average  $223.5^\circ$ , which is quite close to one of the plate’s mounting bolts IF2, located at  $225^\circ$ . The opposite signs of the glitch amplitudes of VBB V and VBB W suggests a deformation relatively symmetrical with respect to the IF2 azimuth, while the low amplitude glitch on VBB U suggests the latter to be much reduced between the two other IFs. This glitch is therefore compatible with a radial deformation of the mounting bolts IF2. Further analysis on the impact of the thermo-elastic stresses in the VBB sphere and the resultant glitch generation will however be demonstrated in a future publication.

**Table 2.** Glitch example from Figure 6: calculated amplitude and geometry parameters.

Component	Glitch amplitude ( $\text{nm/s}^2$ )	Precursor amplitude (nm)	Tilt (nrad)	Apparent radius $r$ (m)
U	1.48	0.58	-0.46	-1.270
V	179.37	-2.44	-55.4	0.044
W	-258.7	3.03	80.0	0.038

During the night very small but also large rotation radii are found, likely resulting from internal sphere deformation triggered by thermal effects, as discussed previously. During the day however, the rotation radii of the glitches are more stable and in the range 10–30 cm, suggesting an external source and therefore rigid tilt of SEIS, likely generated by the atmospheric activity.

### 6.2 Loading with Arm

The InSight mission includes the Heatflow and Physical Properties Probe (HP<sup>3</sup>, Spohn et al., 2018) that includes a probe (the ”mole”) intended to hammer itself 3-5 m into the regolith. The mole has had difficulty getting started, and so the lander’s Instrument Deployment Arm (IDA) has been pressed into service to help. On several occasions, the IDA has pushed down on either the regolith or the mole itself. When the IDA pushes down, it induces an elastic response in the regolith, deforming the surface into a funnel shape, inducing a tilt at the seismometer about 1.2 m away. This tilt of about 70 nrad is clearly observable on both the SP and VBB sensors in Figure 9 as steps in the horizontal accelerations.

In this example, at the start of the command sequence the IDA was pushing down lightly on the mole, and was given four commands: 1) move up to get off the mole, 2) move horizontally in mid-air, 3) move down to just above the mole, and 4) move down to reload the mole with a downward force.

We see in the seismometer data the first move up and the resulting tilt up to the NE. The arm resonates after it loses contact with the mole, and we see that as the 4 Hz ringing in the seismometer

674 data. The seismometer does not have a significant response to the horizontal move. Then on the  
 675 third move, it appears that the IDA actually touched the mole while stopping and then rebounded  
 676 and resonated while hovering in mid-air just above the mole. Finally the IDA moves down to load  
 677 the mole and we see a tilt down to the NE at the seismometer.

678 We also see several glitches that happen at the same time as the IDA motions. One of the tell-tale  
 679 signs of a glitch is when we observe an offset in acceleration in the vertical component. Note that a  
 680 tilt and a glitch can have the same signature in acceleration for the horizontal components. Another  
 681 indication of a glitch in this case is that the BHE-component shows steps of the same sign for both  
 682 the unloading and loading. Two of the glitches appear to involve the whole sensor assembly as they  
 683 are seen on both the VBB and SP. Other glitches seem to be limited to one or more components of  
 684 the VBB.

### 685 6.3 Atmospheric Pressure

686 Pressure effects such as convective vortices ("pressure drops" or "dust devils", e.g. Lorenz et al.,  
 687 2015; Kenda et al., 2017, turbulence in the atmospheric planetary boundary layer (Murdoch et al.,  
 688 2017; Banfield et al., 2020), gravity waves (Spiga et al., 2018; Garcia et al., 2020) and acoustic waves  
 689 (Martire et al., under review in this issue) are generating signals on SEIS components from 0.5 mHz  
 690 up to about 2 Hz. Among these pressure related perturbations, convective vortices are generating the  
 691 largest physical signals observed on SEIS. Their dominant period, as observed by SEIS, can be close  
 692 to the one of the glitches depending on their size, distance to SEIS and wind speed (Murdoch et al.,  
 693 under review in this issue). These strong signals are observed on horizontal SEIS components due to  
 694 effects like ground tilt and therefore are good candidates to be detected as glitches.

## 695 7 Conclusions

696 We have developed a possible model for the generation of glitches and their associated high-  
 697 frequency precursors that occur simultaneously with the glitch onset. In this model, glitches represent  
 698 steps in the acceleration sensed by the individual sensors convolved with the instrument responses  
 699 whilst glitch precursors represent steps in the displacement sensed by the individual sensors convolved  
 700 with the instrument responses. We use our model to develop different algorithms for the glitch  
 701 detection that are all able to identify most of the high amplitude glitches for both the VBB and  
 702 SP seismometers (Section 2, Fig. 2). Based on our model we furthermore demonstrate that most  
 703 glitches are thermally-driven (Section 3, Figs. 3–5). Such glitches likely represent SEIS-internal tilts  
 704 that differ across the individual sensors and hence produce glitches on the vertical components, an  
 705 observation that cannot be reconciled with a tilt of the SEIS package. Only a small fraction of all  
 706 observed glitches can be explained by the whole SEIS instrument physically tilting. We illustrate  
 707 these two cases of glitch production in Figure 8. The removal of glitches and precursors, based on our  
 708 model, has proven successful in many cases for both seismometers (Section 4, Figs. 6–7). Of course,  
 709 there remain glitches and precursors especially of smaller amplitudes that we can not sufficiently well  
 710 fit and therefore confidently remove. Nevertheless, our model for the generation of glitches and their  
 711 associated precursors has proven successful and users of InSight's seismic data should therefore benefit  
 712 from deglitching the data following our considerations presented in this study.

713 As no glitch removal algorithm can warrant a perfect clean-up of all glitches and their precursors,  
 714 we decided to not provide a deglitched time series of all available data. Instead, we have assembled our  
 715 algorithms for glitch detection (Section 2), glitch polarization analysis (Section 3) and glitch removal  
 716 (Section 4) into one Python / ObsPy toolbox. The package also holds MatLab scripts to perform  
 717 glitch detection and removal tasks as presented. Its link is: [https://pss-gitlab.math.univ-paris-](https://pss-gitlab.math.univ-paris-diderot.fr/data-processing-wg/seisglitch)  
 718 [diderot.fr/data-processing-wg/seisglitch](https://pss-gitlab.math.univ-paris-diderot.fr/data-processing-wg/seisglitch). Documentation is available. Together with this  
 719 code we also provide deglitched data for a selection of seismic events.

## 720 Acknowledgments

721 We acknowledge NASA, CNES, partner agencies and Institutions (UKSA, SSO, DLR, JPL, IPGP-  
 722 CNRS, ETHZ, IC, MPS-MPG) and the operators of JPL, SISMOC, MSDS, IRIS-DMC and PDS for  
 723 providing SEED SEIS data: [http://dx.doi.org/10.18715/SEIS.INSIGHT.XB\\\_2016](http://dx.doi.org/10.18715/SEIS.INSIGHT.XB\_2016). French teams  
 724 acknowledge support from CNES as well as Agence Nationale de la Recherche (ANR-14-CE36-0012-

725 02 and ANR-19-CE31-0008-08). The Swiss contribution in implementation of the SEIS electronics  
726 was made possible through funding from the federal Swiss Space Office (SSO), the contractual and  
727 technical support of the ESA-PRODEX office. The MPS-MPG SEIS team acknowledges funding for  
728 development of the SEIS leveling system by the DLR German Space Agency. FN acknowledges partial  
729 support from the InSight PSP program under grant 80NSSC18K1627. Documentation is available.  
730 This paper is InSight Contribution Number 128.

731 **References**

- 732 Ahern, T. K., Buland, R., Halbert, S., Styles, Ray, Skjellerup, Kris, Casey, Rob, ... Trabant, Chab  
733 (2012). *SEED Reference Manual*. IRIS.
- 734 Allison, M., & McEwen, M. (2000). A post-pathfinder evaluation of areocentric solar coordinates  
735 with improved timing recipes for mars seasonal/diurnal climate studies. *Planetary and Space Sci-*  
736 *ence*, 48(2), 215 - 235. Retrieved from [http://www.sciencedirect.com/science/article/pii/](http://www.sciencedirect.com/science/article/pii/S0032063399000926)  
737 [S0032063399000926](http://www.sciencedirect.com/science/article/pii/S0032063399000926) doi: [https://doi.org/10.1016/S0032-0633\(99\)00092-6](https://doi.org/10.1016/S0032-0633(99)00092-6)
- 738 Banerdt, W. B., Smrekar, S. E., Banfield, D., Giardini, D., Golombek, M., Johnson, C. L., ... Wic-  
739 zorek, M. (2020, February). Initial results from the InSight mission on Mars. *Nature Geoscience*.  
740 doi: 10.1038/s41561-020-0544-y
- 741 Banfield, D., Spiga, A., Newman, C., Forget, F., Lemmon, M., Lorenz, R., ... Banerdt, W. B.  
742 (2020, February). The atmosphere of Mars as observed by InSight. *Nature Geoscience*. doi:  
743 10.1038/s41561-020-0534-0
- 744 Beyreuther, M., Barsch, R., Krischer, L., Megies, T., Behr, Y., & Wassermann, J. (2010, May).  
745 ObsPy: A Python Toolbox for Seismology. *Seismological Research Letters*, 81(3), 530–533. doi:  
746 10.1785/gssrl.81.3.530
- 747 Clinton, J., Giardini, D., Böse, M., Ceylan, S., van Driel, M., Euchner, F., ... Teanby, N. A. (2018,  
748 December). The Marsquake Service: Securing Daily Analysis of SEIS Data and Building the Martian  
749 Seismicity Catalogue for InSight. *Space Science Reviews*, 214(8), 133. doi: 10.1007/s11214-018-0567  
750 -5
- 751 Fayon, L., Knapmeyer-Endrun, B., Lognonné, P., Bierwirth, M., Kramer, A., Delage, P., ... Banerdt,  
752 W. B. (2018, December). A Numerical Model of the SEIS Leveling System Transfer Matrix and  
753 Resonances: Application to SEIS Rotational Seismology and Dynamic Ground Interaction. *Space*  
754 *Science Reviews*, 214(8). doi: 10.1007/s11214-018-0555-9
- 755 Garcia, R. F., Kenda, B., Kawamura, T., Spiga, A., Murdoch, N., Lognonné, P. H., ... Banerdt,  
756 W. B. (2020). Pressure Effects on the SEIS-InSight Instrument, Improvement of Seismic Records,  
757 and Characterization of Long Period Atmospheric Waves From Ground Displacements. *Journal of*  
758 *Geophysical Research: Planets*, e2019JE006278. doi: 10.1029/2019JE006278
- 759 Giardini, D., Lognonné, P., Banerdt, W. B., Pike, W. T., Christensen, U., Ceylan, S., ... Yana, C.  
760 (2020, February). The seismicity of Mars. *Nature Geoscience*. doi: 10.1038/s41561-020-0539-8
- 761 InSight Mars SEIS Data Service. (2019). *SEIS Raw Data, Insight Mission*. IPGP, JPL, CNES, ETHZ,  
762 ICL, MPS, ISAE-Supaero, LPG, MFSC. doi: <https://doi.org/10.18715/SEIS.INSIGHT.XB.2016>
- 763 InSight Marsquake Service. (2020). *Mars seismic catalogue, insight mission; v2 2020-04-01*. ETHZ,  
764 IPGP, JPL, ICL, ISAE-Supaero, MPS, Univ. Bristol. Retrieved from [http://www.insight.ethz](http://www.insight.ethz.ch/seismicity/catalog/v2)  
765 [.ch/seismicity/catalog/v2](http://www.insight.ethz.ch/seismicity/catalog/v2) doi: 10.12686/a7
- 766 Kenda, B., Lognonné, P., Spiga, A., Kawamura, T., Kedar, S., Banerdt, W. B., ... Golombek,  
767 M. (2017, October). Modeling of Ground Deformation and Shallow Surface Waves Generated by  
768 Martian Dust Devils and Perspectives for Near-Surface Structure Inversion. *Space Science Reviews*,  
769 211(1-4), 501–524. doi: 10.1007/s11214-017-0378-0
- 770 Krischer, L., Megies, T., Barsch, R., Beyreuther, M., Lecocq, T., Caudron, C., & Wassermann, J.  
771 (2015, May). ObsPy: A bridge for seismology into the scientific Python ecosystem. *Computational*  
772 *Science & Discovery*, 8(1), 014003. doi: 10.1088/1749-4699/8/1/014003
- 773 Lagrange, J.-L. (1813). *Theorie des fonctions analytiques. nouvelle edition revue et augmentee par*  
774 *l'auteur*. Veuve Coucier.
- 775 Lognonné, P., Banerdt, W. B., Giardini, D., Pike, W. T., Christensen, U., Laudet, P., ... Wookey, J.  
776 (2019, January). SEIS: Insight's Seismic Experiment for Internal Structure of Mars. *Space Science*  
777 *Reviews*, 215(1). doi: 10.1007/s11214-018-0574-6
- 778 Lognonné, P., Banerdt, W. B., Pike, W. T., Giardini, D., Christensen, U., Garcia, R. F., ... Zweifel,  
779 P. (2020, February). Constraints on the shallow elastic and anelastic structure of Mars from InSight  
780 seismic data. *Nature Geoscience*. doi: 10.1038/s41561-020-0536-y
- 781 Lorenz, R. D., Kedar, S., Murdoch, N., Lognonné, P., Kawamura, T., Mimoun, D., & Bruce Banerdt,  
782 W. (2015, December). Seismometer Detection of Dust Devil Vortices by Ground Tilt. *The Bulletin*  
783 *of the Seismological Society of America*, 105, 3015-3023. doi: 10.1785/0120150133
- 784 Martire, G. R. F., Léo, Rolland, L., Spiga, A., Lognonné, P. H., Banfield, D., & Banerdt, W. B.  
785 (under review in this issue). Martian infrasound: numerical modeling and analysis of InSight's  
786 data. *Journal of Geophysical Research: Planets*.

- 787 Murdoch, N., Kenda, B., Kawamura, T., Spiga, A., Lognonné, P., Mimoun, D., & Banerdt, W. B.  
788 (2017, October). Estimations of the Seismic Pressure Noise on Mars Determined from Large Eddy  
789 Simulations and Demonstration of Pressure Decorrelation Techniques for the InSight Mission. *Space*  
790 *Science Reviews*, *211*, 457-483. doi: 10.1007/s11214-017-0343-y
- 791 Murdoch, N., Spiga, A., Lorenz, R., Garcia, R., Perrin, C., Widmer-Schmidrig, R., ... Banerdt, W.  
792 (under review in this issue). Constraining Martian regolith parameters and vortex trajectories from  
793 combined seismic and meteorological measurements. *Journal of Geophysical Research: Planets*.
- 794 Pou, L., Mimoun, D., Lognonne, P., Garcia, R. F., Karatekin, O., Nonon-Latapie, M., & Llorca-  
795 Cejudo, R. (2019, February). High Precision SEIS Calibration for the InSight Mission and Its  
796 Applications. *Space Science Reviews*, *215*(1), 6. doi: 10.1007/s11214-018-0561-y
- 797 Rossum, G. (1995). *Python Reference Manual* (Tech. Rep.). Amsterdam, The Netherlands: CWI  
798 (Centre for Mathematics and Computer Science).
- 799 Scholz, J.-R., Barruol, G., Fontaine, F. R., Sigloch, K., Crawford, W., & Deen, M. (2017). Orienting  
800 Ocean-Bottom Seismometers from P-wave and Rayleigh wave polarisations. *Geophysical Journal*  
801 *International*, *208*(3), 1277–1289. doi: 10.1093/gji/ggw426
- 802 Spiga, A., Banfield, D., Teanby, N. A., Forget, F., Lucas, A., Kenda, B., ... Banerdt, W. B. (2018,  
803 October). Atmospheric Science with InSight. *Space Science Reviews*, *214*(7). doi: 10.1007/s11214  
804 -018-0543-0
- 805 Spohn, T., Grott, M., Smrekar, S. E., Knollenberg, J., Hudson, T. L., Krause, C., ... Banerdt, W. B.  
806 (2018, August). The Heat Flow and Physical Properties Package (HP3) for the InSight Mission.  
807 *Space Science Reviews*, *214*(5). doi: 10.1007/s11214-018-0531-4

## Figures

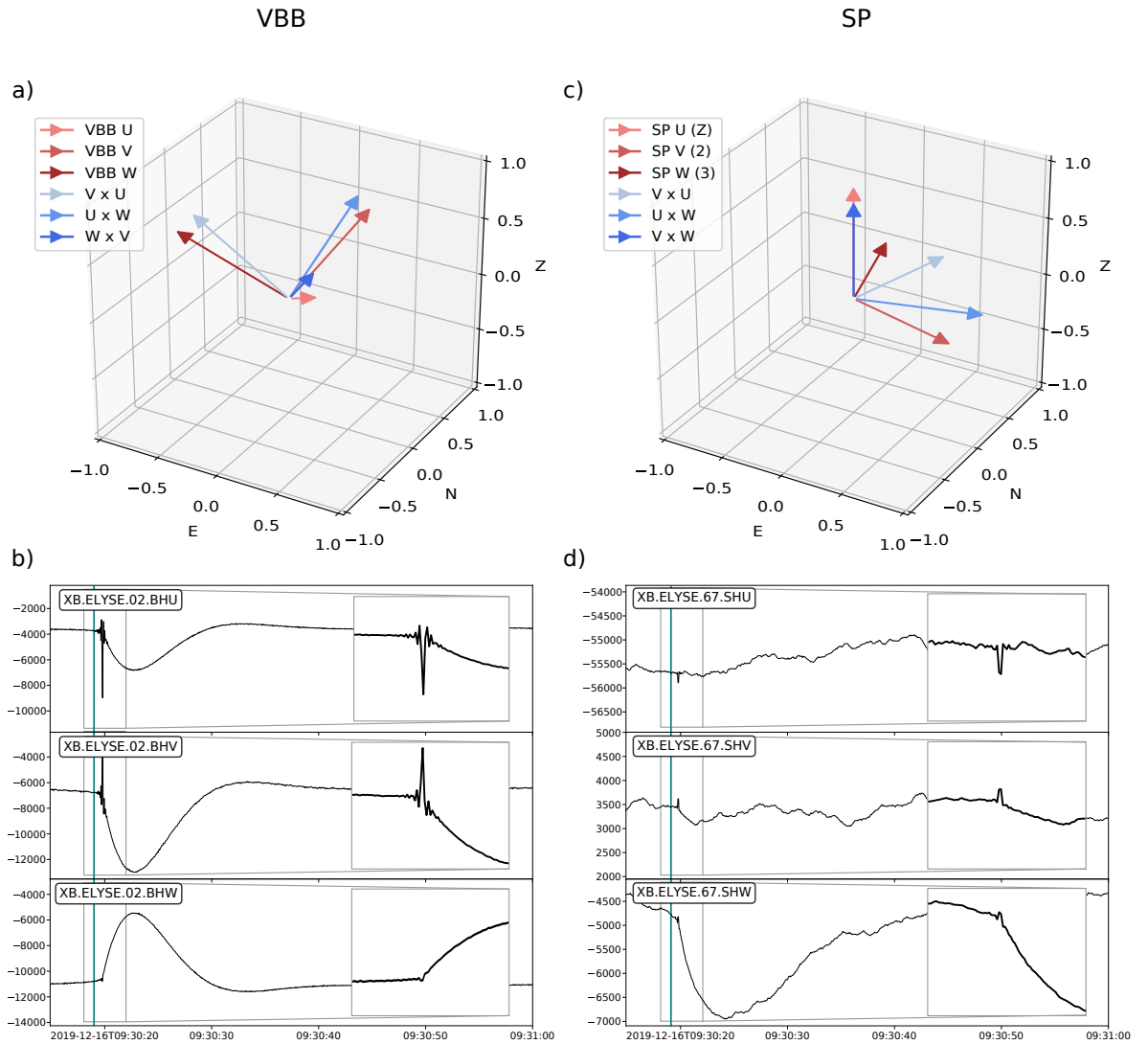


**Figure 1.** Sensitive directions (red arrows) of the two three-component seismometers that are part of the SEIS package; a) VBB, c) SP. Blue vectors are the pairwise vector cross-products of the sensor directions for the VBBs and SPs, respectively. Since the sensitive axes of the instruments are not orthogonal, the cross products of two sensors do not coincide with the sensitive direction of the third component (see Section 3.1 for details and values of sensor orientations). Multi-component glitch example at 2019-12-16T09:30:19 (sol 374) occurring on both b) VBB, and d) SP. Green lines refer to detected glitch onset after deconvolution method (Section 2.1). Note there is no glitch visible on SP U and SP V. The glitch precursors (inlays) are visible on all six seismic components, however much less on SP.

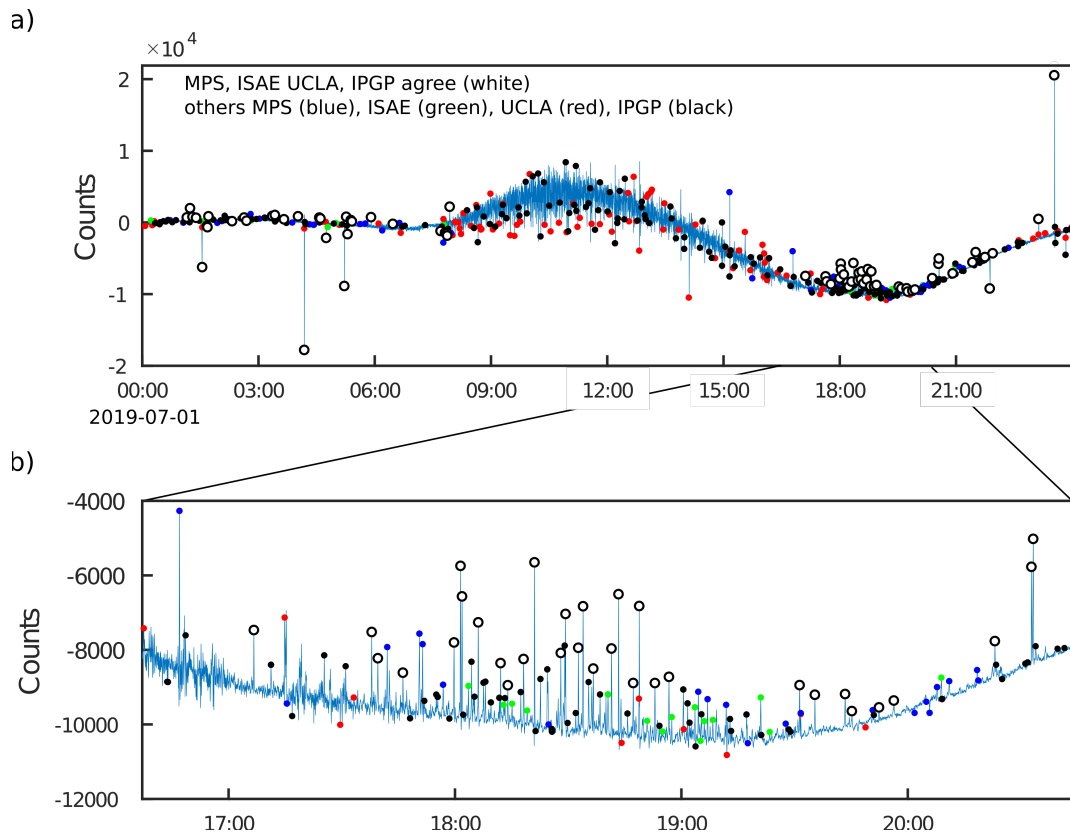


**Figure 2.** a) Comparison between glitches detected on July 1 2019 (sol 211) by our four sub-groups: MPS, ISAE, IPGP, and UCLA. White circles are common glitches for all groups. Color coded symbols correspond to glitches for the different groups that are not common to all. Those common to sub-groups are plotted on top of each other and so the last plotted is shown. b) Zoomed-in section showing that as the threshold for declaring a glitch, either in terms of signal-to-noise or correlation with the template, is lowered, results differ markedly, and some possible candidate glitches may have been missed.

## One-component Glitches

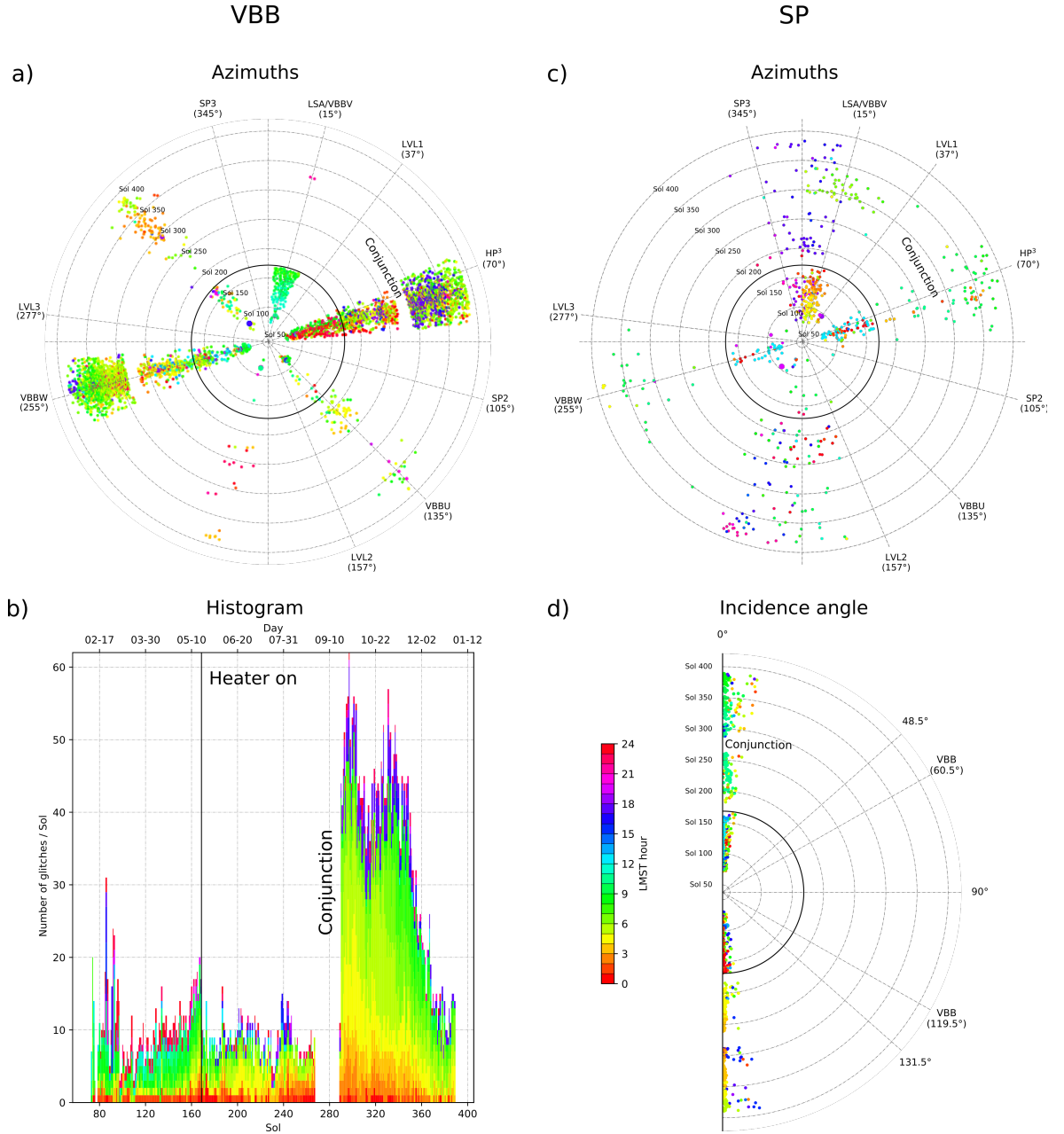


**Figure 3.** One-component glitches for VBB and SP as detected by one of our detection algorithms (MPS) for 2019: a) VBB one-component glitches. The azimuths align with the VBB components. Incidence angles are as expected  $INC \sim 48^\circ/132^\circ$  (not shown, see text for details), b) histogram of a). Note the rate change of glitches after heater activation (sol 168) and conjunction (sols 267–288), the latter mostly caused by VBB W, c) SP one-component glitches for the horizontal components SP V and SP W, and d) one-component glitches for (almost) vertical SP U component. Color code refers to local mean solar time (LMST, in hours) of glitch onsets.

### Multi-component Glitches

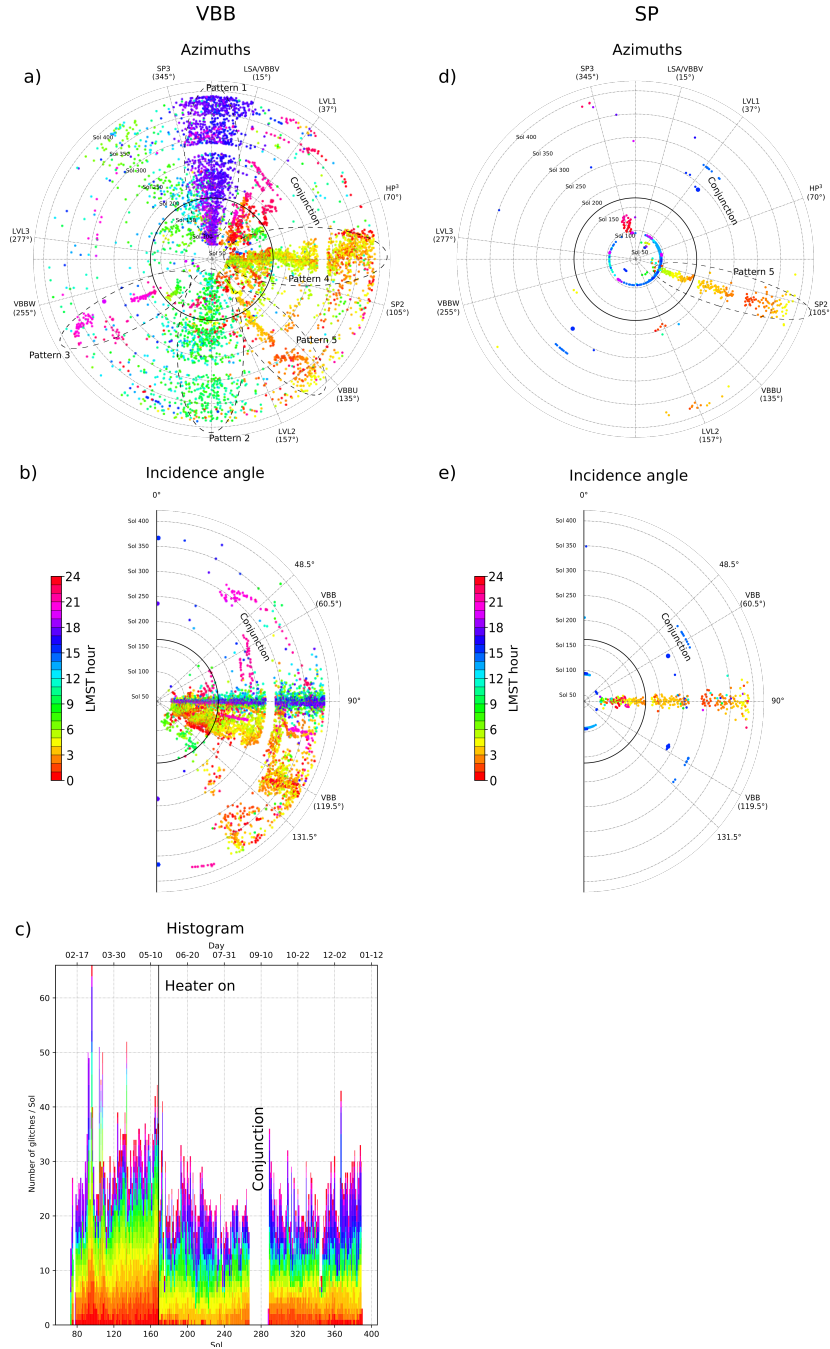


**Figure 4.** Multi-component glitches for VBB and SP as detected by one of our detection algorithms (MPS) for 2019: a) VBB glitch azimuths. Marked are the five most prominent patterns (see text for details). Note only the incidence angles for patterns 1 and 2 point into the horizontal plane (not shown, see text for details), b) VBB glitch incidence angles, generally pointing in the horizontal plane for patterns 1 and 2 but not for the other patterns, c) histogram of a) and b). Note the rate change of night time glitches after heater activation (sol 168), d) SP glitch azimuths. Pattern 5, that also occurs on the VBBs, is marked. The blue dots mostly refer to false glitch detections caused by HP<sup>3</sup>-hammering sessions and InSight’s robotic arm movements, e) SP glitch incidence angles, demonstrating that multi-component SP glitches occur only among the horizontal SP V and SP W components. Color code refers to local mean solar time (LMST, in hours) of glitch onsets.

## Glitches on both VBB and SP

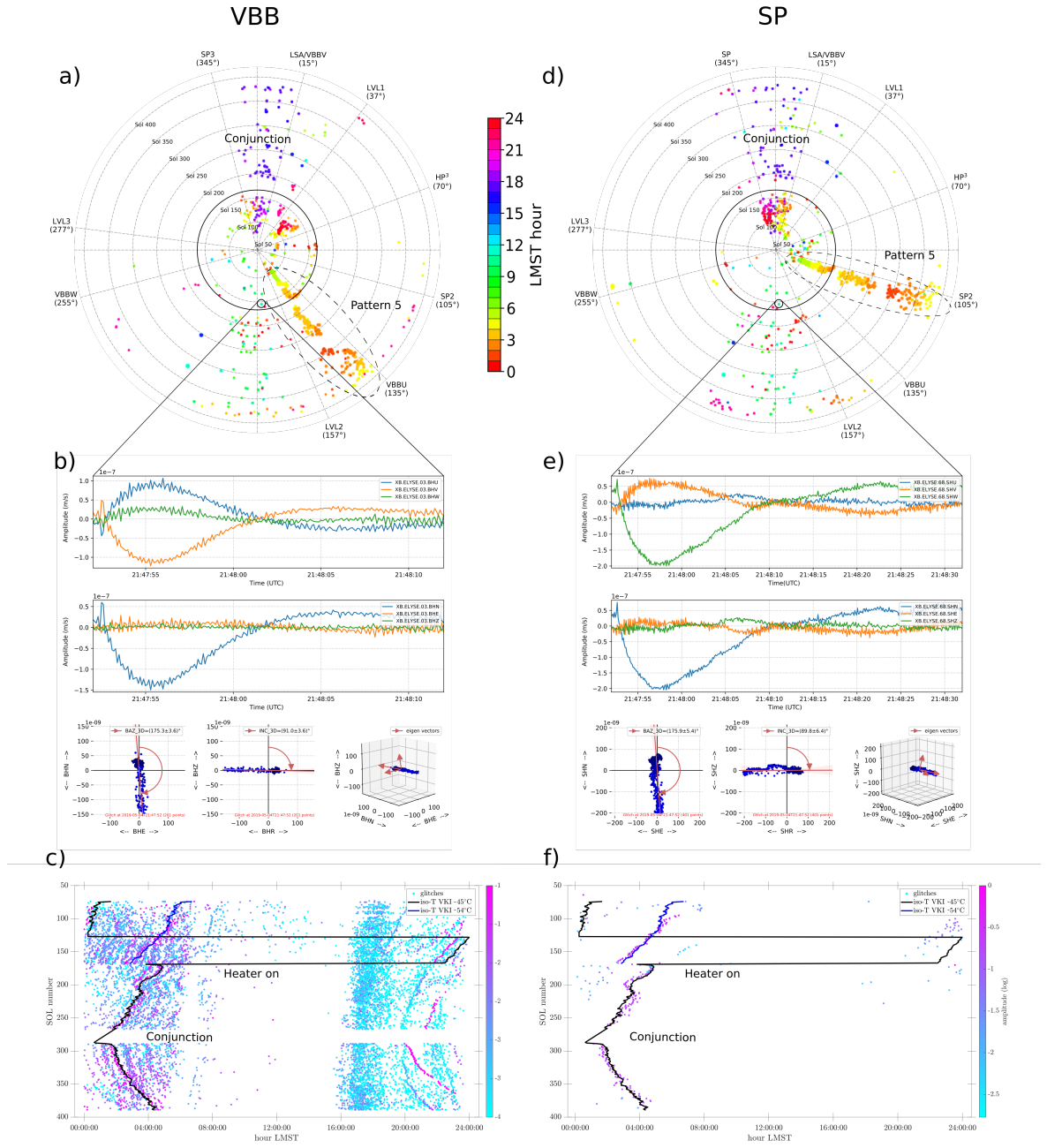


**Figure 5.** a,d) Glitches in 2019 that occurred simultaneously on VBB and SP. Glitch azimuths agree for patterns 1 and 2 but not for pattern 5. Color code refers to local mean solar time (LMST, in hours) of glitch onsets, b,e) example of our polarization analysis of the same glitch for VBB and SP, c,f) normalised glitch amplitudes as a function of sols over hours of sol (different detection method than in sub-plots a-d). Note how the SCIT A (scientific temperature sensor A, channel 03.VKI) iso-curve at  $-54^{\circ}\text{C}$  matches the glitches that correspond to pattern 5, thus supporting thermal causes as primary glitch generators for this pattern.

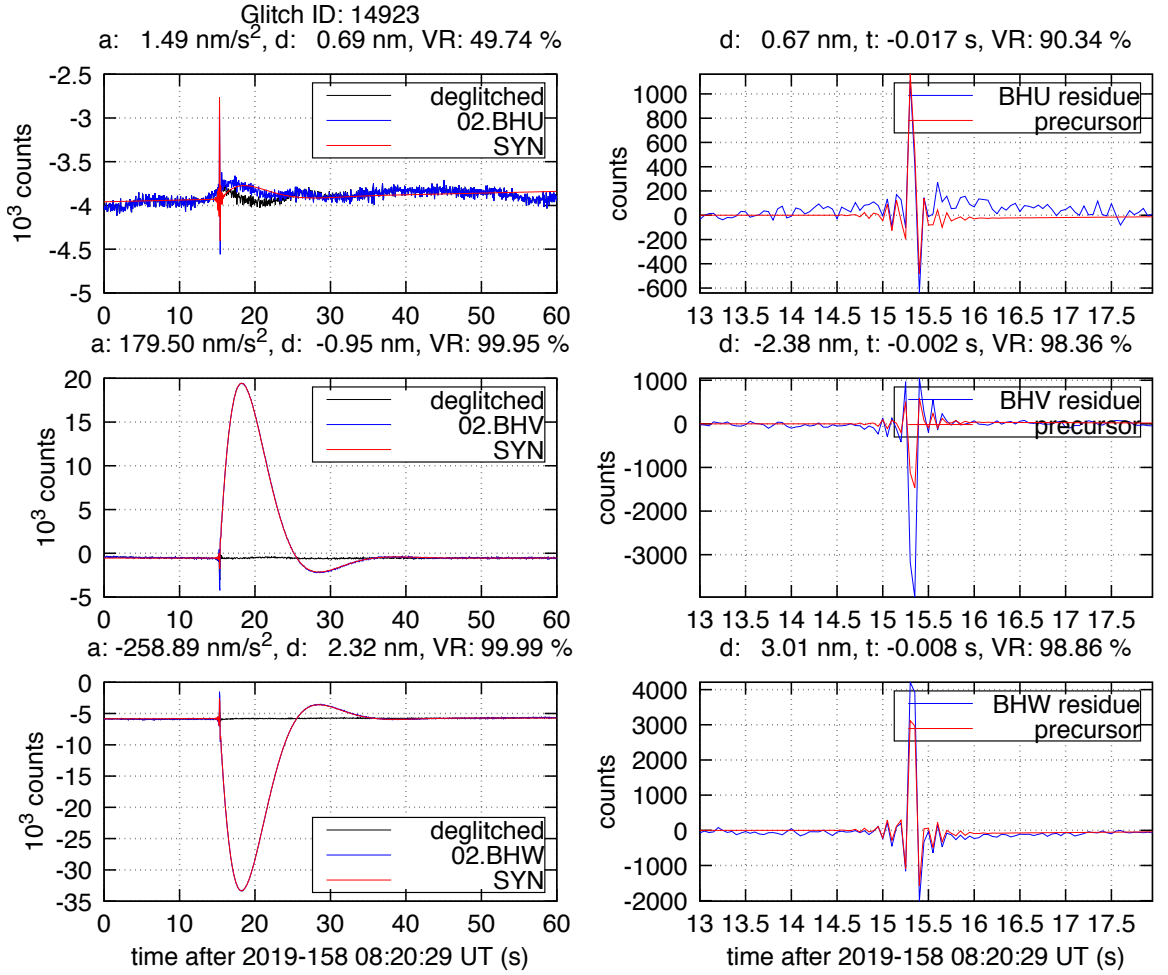


**Figure 6.** Automated glitch removal for VBB at work: a) we fitted the glitches (blue lines) with the nominal VBB responses to a step in acceleration (red lines). The deglitched data (black lines) were obtained by subtracting only the scaled version of the synthetic glitches, i.e. without offset and linear trend parameters, from the original data. b) high-frequency precursors (red lines) were modeled with the nominal VBB responses to a step in displacement and fitted to the deglitched data of a) (blue lines). Note that our glitch model allows to fit both the glitch and the glitch precursors very well, even if small mismatches remain.

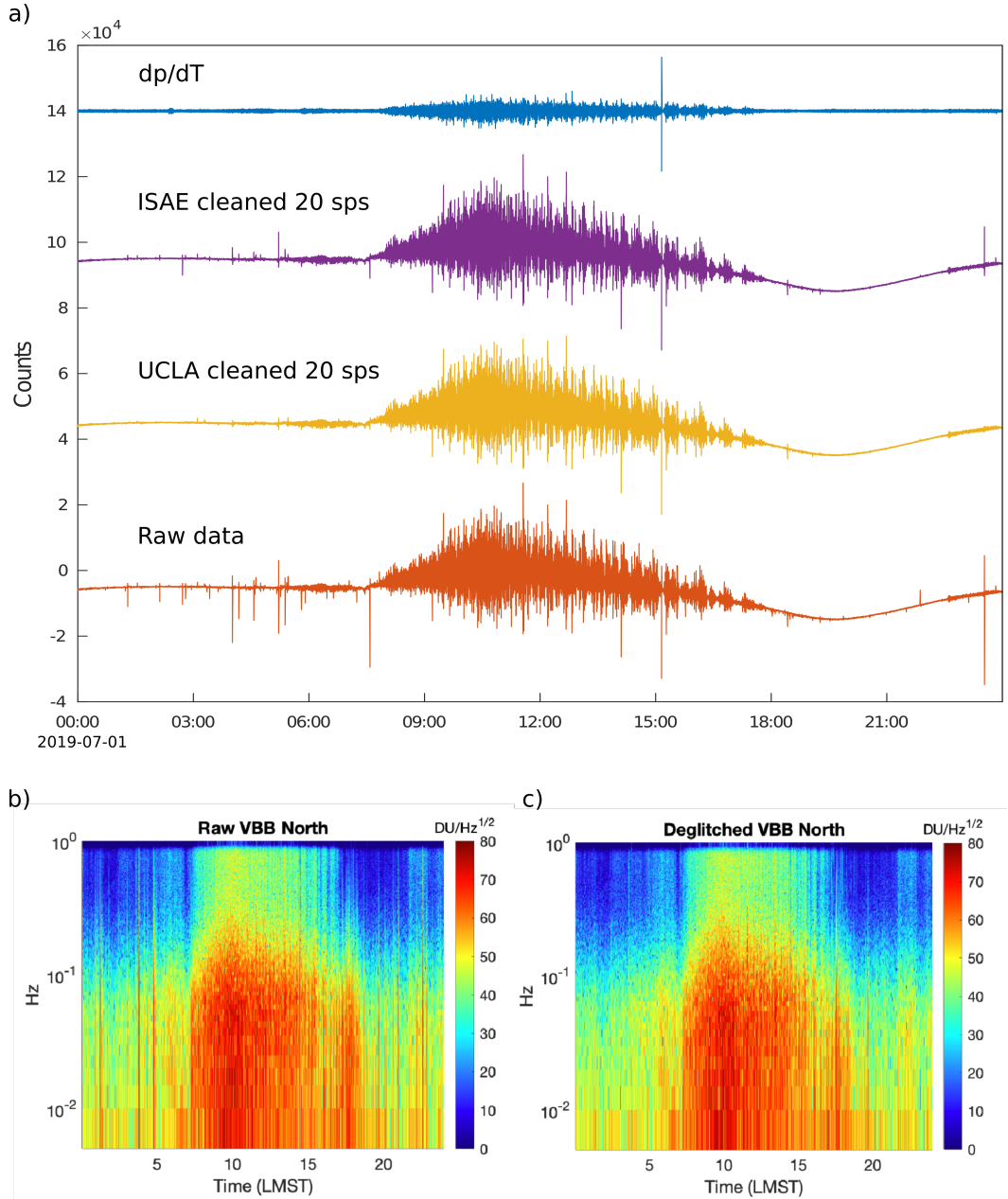


**Figure 7.** a) Raw time series data for 2019-07-01 (sol 211) of the time-derivative of pressure channel 03.BDO (10 sps), VBB 02.BHW data cleaned from glitches (ISAE) and cleaned from glitches+precursors (UCLA), and original VBB 02.BHW raw data. The large transient seen in the pressure data at  $\sim 15:00$  LMST survives the cleaning as it has the morphology of the derivative of the glitch template. A number of the precursors have been removed but not all, and other transients remain that are not explained in the glitch-precursor-pressure framework, b,c) comparison of spectrograms in the 0.005–1 Hz (1–200 s) bandwidth from before (left) and after (right) deglitching using the IPGP-method: Note that the spectrograms show the VBB N-component, so the UVW data were first deglitched and then rotated to ZNE for the spectrogram calculations.

PHILIPPE: With the exception of a few glitches not removed due to their significant difference with the proposed model, those removed allow a cleaning of the spectrogram down to 0.05 Hz. Note that in several cases, glitches are associated with a burst of long-period energy, which suggest glitch triggering by this background, as described in the next section.

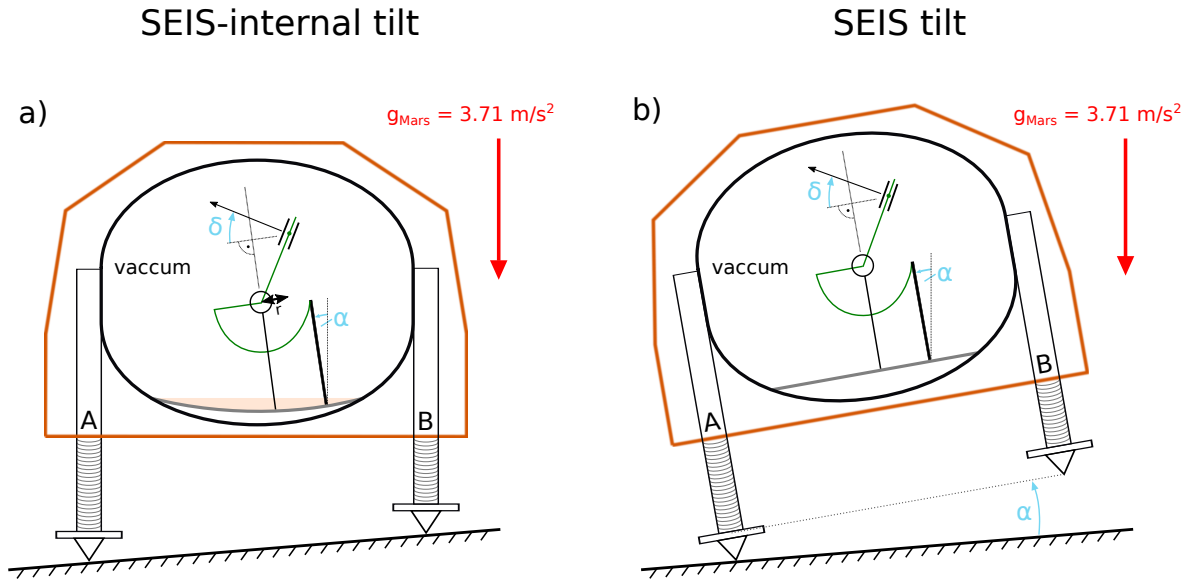


**Figure 8.** Simplified sketch of a cross-section through the instrument package SEIS showing only one VBB sensor: a) SEIS-internal tilt  $\alpha$  caused e.g. by the plate that supports the VBB sensors bending (grey line and orange area). Each VBB sensor (only one illustrated) may see a different tilt, all together combining to yield a non-zero glitch on the (reconstructed) vertical component ( $INC \neq 90^\circ$ ). We suspect such effects to be the primary reason for thermally-caused multi-component glitches such as shown in patterns 3–5 (Fig. 4). b) SEIS tilt  $\alpha$ , corresponding to a true, rigid motion of the whole instrument. Our analysis suggests that the minority of glitches, e.g. patterns 1–2 (Fig. 4), are caused by this scenario. Note that in both cases the VBB sensors may experience a tilt and a displacement (see text for details). Similar considerations apply for the SP sensors that are not shown but mounted on the leveling system support structure (Fayon et al., 2018). For a more detailed and accurate illustration of the SEIS sensor assembly, see Lognonné et al. (2019).  $\delta$ : VBB sensor dip  $\sim -30^\circ$ .

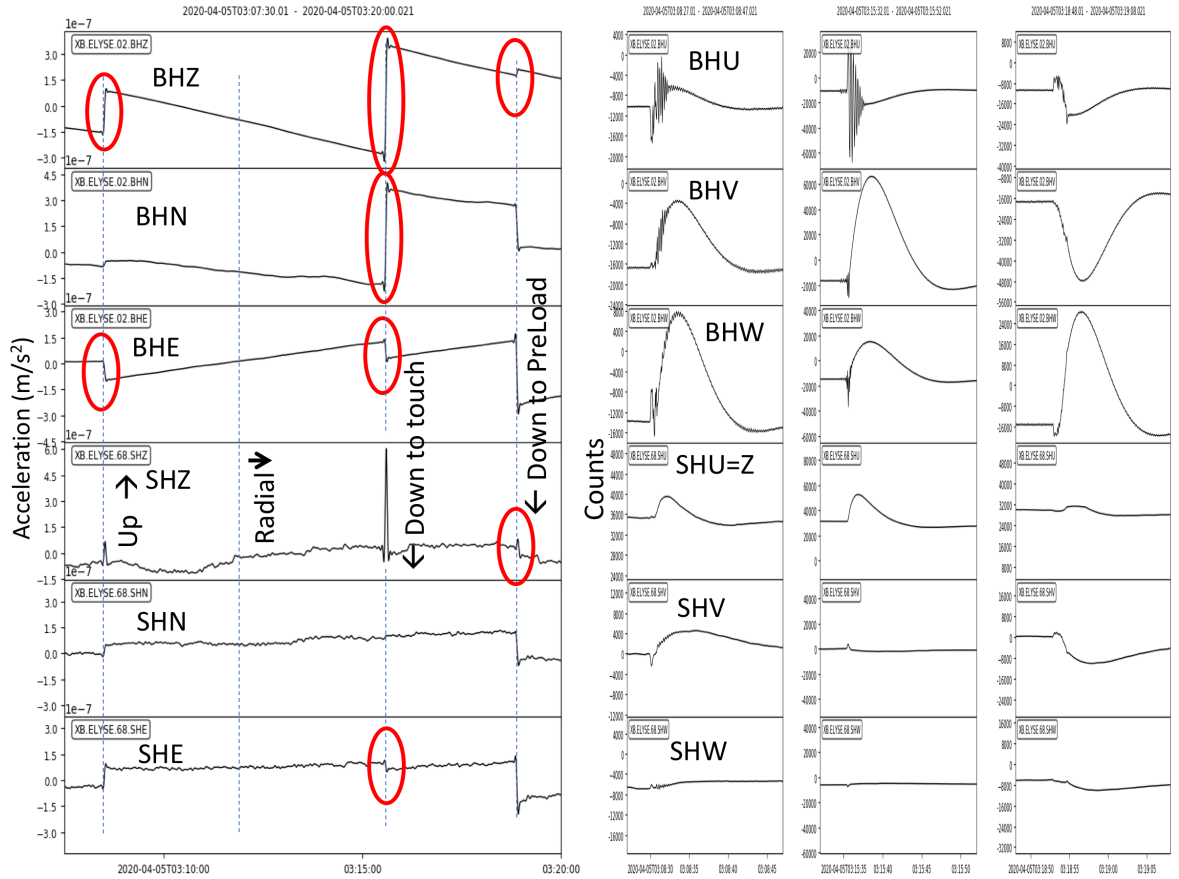


**Figure 9.** VBB and SP data during Instrument Deployment Arm (IDA) pushing on the HP<sup>3</sup>-Mole. The arm started the sequence while pushing down on the Mole. The arm motions are described in the text. Likely glitches are identified with red ellipses in the Z, N, E plots on the left for VBB (top) and SP (bottom). On the right, 20 seconds of the raw U, V, W components (in counts, instrument response not removed) for the first, third, and fourth moves are shown. On many of them, the canonical displacement spike followed by the tilt signature is present.

809 **Supplementary Information**

- 810 • SI1: Lists of glitches detected by the different methods
- 811 • SI2: Mathematical description of glitch plus precursor origins